Matter

Article

Efficient oral insulin delivery with sustained release by folate-conjugated metal-organic framework nanoparticles

Graphical abstract

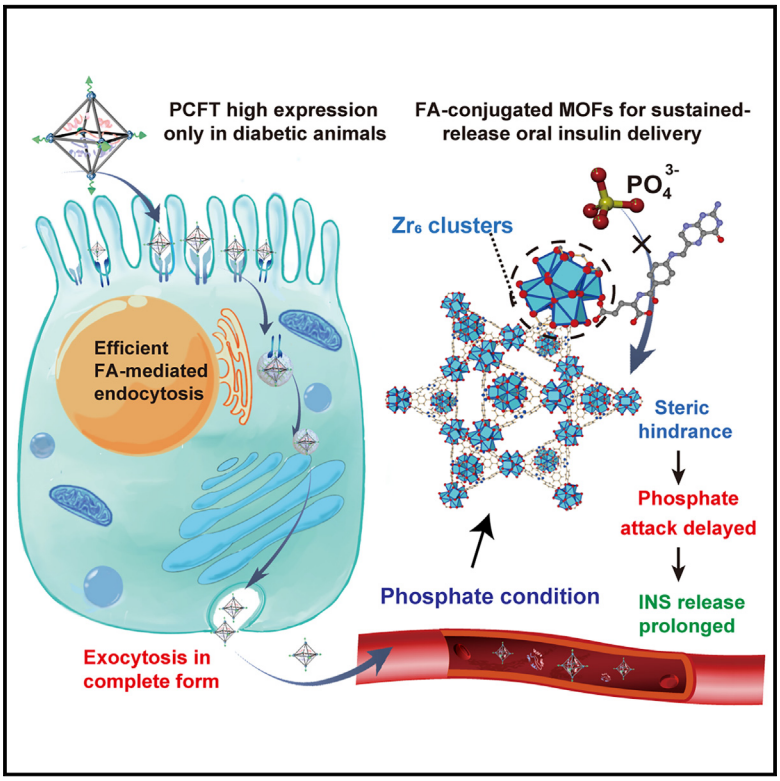

Highlights

- Sustained-release oral insulin delivery by folate-conjugated MOF nanoparticles
- Overcoming intestinal epithelial barriers via PCFT-mediated epithelial transport
- Selectively hypoglycemic effect in diabetics with reduced hypoglycemia risk
- Extraordinary oral bioavailability and extended duration of action of insulin

Authors

Jun-Jie Zou, Qing Chen, Joshua Phipps, ..., Wanyi Tai, Shengqian Ma, Jian Tian

Correspondence

shengqian.ma@unt.edu (S.M.), jian.tian@whu.edu.cn (J.T.)

In brief

By coordinating folate molecules to open coordination sites of metal clusters in Zr-based metal-organic framework (MOF) nanoparticles, we fabricate an efficient sustained-release oral insulin delivery system. This nanoplatform allows oral insulin delivery exclusively within diabetic animals, enabling precise modulation of the release site and rate of insulin *in vivo*. Consequently, it achieves a comprehensive 48-h coverage for blood sugar control and an extraordinary oral bioavailability of 35.5%. This study provides a new strategy for sustained and controlled oral delivery of biological macromolecules.

Improvement
Enhanced performance with innovative design or material control

Zou et al., 2025, Matter *8*, 101948
March 5, 2025 © 2024 Elsevier Inc. All rights are reserved, including those for text and data mining, AI training, and similar technologies.
https://doi.org/10.1016/j.matt.2024.101948

CellPress

Please cite this article in press as: Zou et al., Efficient oral insulin delivery with sustained release by folate-conjugated metal-organic framework nanoparticles, Matter (2024), https://doi.org/10.1016/j.matt.2024.101948

Matter

CellPress

Article

Efficient oral insulin delivery with sustained release by folate-conjugated metal-organic framework nanoparticles

Jun-Jie Zou,[1,2,3] Qing Chen,[1,2] Joshua Phipps,[4] Yu Zhao,[1,2] Xudong Qin,[1,2] Wanyi Tai,[2] Shengqian Ma,[4,*] and Jian Tian[1,2,5,*]

[1]Department of Cardiovascular Surgery, Zhongnan Hospital of Wuhan University, School of Pharmaceutical Sciences, Wuhan University, Wuhan 430071, China

[2]Key Laboratory of Combinatorial Biosynthesis and Drug Discovery (MOE), School of Pharmaceutical Sciences, Wuhan University, Wuhan 430071, China

[3]Department of Pharmacy, Union Hospital, Tongji Medical College, Huazhong University of Science and Technology, Wuhan 430022, China

[4]Department of Chemistry, University of North Texas, Denton, TX 76201, USA

[5]Lead contact

*Correspondence: shengqian.ma@unt.edu (S.M.), jian.tian@whu.edu.cn (J.T.)

https://doi.org/10.1016/j.matt.2024.101948

PROGRESS AND POTENTIAL Long-acting oral delivery of therapeutic proteins/peptides poses one of the biggest challenges in drug delivery. This study reports a simple yet highly efficient oral formulation based on folate-conjugated Zr-MOF nanoparticles, which realizes sustained insulin release selectively in diabetics and extraordinary bioavailability. The acid-resistant Zr-MOF nanocarriers protect insulin from acid and enzymatic degradation in the harsh gastrointestinal environment. By utilizing functional folate molecules to occupy the vacant coordination sites of metal clusters in Zr-MOF, MOF nanocarriers can not only achieve specific intestinal transport but also realize highly controlled insulin release behaviors *in vivo* with reduced hypoglycemia risk, avoiding rapid disintegration and burst drug release. The extended drug duration and improved efficacy of MOF-based oral protein/peptide delivery nanosystems offer translational opportunities for effective glycemic management in the long term.

SUMMARY

Oral protein/peptide delivery systems have garnered global interest due to their potential to provide substantial benefits to patients. However, their clinical translation has been impeded by challenges pertinent to poor intestinal permeability, acid instability, and the short half-life of proteins/peptides. Here, we report a simple, efficient, and sustained-release oral insulin delivery system based on folic acid (FA)-conjugated acid-resistant metal-organic framework (MOF) nanoparticles with high drug-loading capacity. The FA conjugation on MOF (PCN-777) nanoparticles not only selectively augmented intestinal transportation efficiency in diabetic animals via upregulated intestinal FA transporter-mediated endocytosis but they also tuned PCN-777 disintegration in the phosphate-rich bloodstream environment to sustain long-acting basal insulin release kinetics within a narrow therapeutic range. In diabetic animal models, the FA-PCN-777 oral insulin delivery nanosystem exhibited a smooth hypoglycemic effect for up to 48 h and a markedly high bioavailability of 35.5%, representing a potential long-acting oral formulation with reduced hypoglycemia risk.

INTRODUCTION

Protein and peptide drugs have revolutionized the therapeutic landscape of various chronic and acute diseases with their high affinity, high specificity, and low toxicity.[1,2] Nevertheless, most approved therapeutic proteins and peptides have short half-lives and are administrated exclusively via continuous subcutaneous injection.[3,4] For instance, the duration of regular insulin (INS) action is generally between 4 and 8 h, thus requiring patients with severe diabetes to take 2–4 INS injections per day to manage blood glucose levels (BGLs) effectively.[5] Unfortunately, repeating these injections daily causes physical pain and psychological stress, which can be intolerable for those with chronic diabetes.[6,7] In particular, the potential for substandard drug administration may lead to suboptimal glycemic control[8,9] and even cardiovascular disease risk.[10] To address the transient

All rights are reserved, including those for text and data mining, AI training, and similar technologies.

effects of conventional INS, researchers have explored structural modifications of INS to extend the duration of the drug's action. INS glargine and INS degludec were recognized for their long-acting basal INS supply and smooth time-action profile, successfully prolonging the INS duration beyond 36 h, with reduced hypoglycemia risk. However, the persistent pain associated with constant injections remains unresolved for patients despite all these advancements. Consequently, it is essential to develop non-invasive INS delivery systems with long-acting basal INS release kinetics and high bioavailability.[11,12]

Oral administration, offering low invasiveness and high patient compliance, represents a transformative solution for chronic disease treatment.[13,14] In 2019, oral semaglutide tablets (Rybelsus) became the first Food and Drug Administration-approved oral protein/peptide drug for type 2 diabetes, marking a significant milestone.[15] Although Rybelsus effectively manages hypoglycemia and can lead to weight loss, the clinical application was still limited by the low bioavailability of ~1.4%.[16] Such low bioavailability is due primarily to the presence of multiple physiological barriers in the gastrointestinal tract (GIT), including ultra-acidic pH, proteolytic enzymes, mucus layer, and intestinal epithelium.[17] To improve the oral bioavailability of protein/peptide drugs, researchers have screened out numerous nanocarriers that can overcome the above physiological barriers to a certain extent, including liposomes, polymeric nanoparticles (NPs), and silicon NPs.[18–23] In addition, some efforts were devoted to prolonging the release of INS from nanocarriers, extending the action duration of INS up to 24 h.[24–29] Still, current oral delivery methodologies confront difficulties in consistently attaining high bioavailability and prolonged durations of INS action (Table S1). Incorporating multiple essential functions, including efficient drug loading, protein protection, sustained and controlled release, and effective permeation, into a simple and safe oral delivery system remains challenging.

Among various nanocarriers, nanoscale metal-organic frameworks (nMOFs) are a relatively new class of highly porous nanomaterials that combine the advantages of high drug loading capacity (LC), good biocompatibility and biodegradability, controllable drug release, and easy modification.[30–32] Therefore, nMOFs have received extensive attention in drug delivery in recent years.[33–35] For instance, in a recent work, Chen et al. developed a pH-triggered self-disintegrating capsule based on a zwitterionic hydrogel-coated MOF for oral peptide delivery that can significantly increase endogenous INS secretion.[36] Additionally, our group previously reported the development of a transferrin-coated acid-resistant Zr-MOF oral INS delivery system with efficacious protein protection and intestinal transportation.[37] Nonetheless, it is noteworthy that most nMOFs display limited structural integrity when subjected to physiological conditions, as documented in existing research, with a typical INS duration of ~1–10 h (Table S1). Furthermore, the rapid initial release of INS may engender unfavorable outcomes, including hypoglycemia.[36–39] Despite advancements realized in augmenting the oral bioavailability of INS through our preceding transferrin-coated Zr-MOF NPs, the intrinsic propensity of nMOFs undergoing rapid degradation within the biological milieu remains unchanged.[40] This imparts substantial challenges to their applicability in the biomedical context. Consequently, we endeavor to engineer precise MOF-based oral INS delivery systems that can effectively penetrate the intestinal epithelial barrier while meticulously governing drug-release kinetics, closely mimicking the *in vivo* profile of endogenous INS secretion.

Our previous study revealed that the disintegration of Zr-MOFs *in vivo* was specifically triggered by the phosphate environment, primarily attributable to the competition for the excessive Zr cluster coordination sites between the phosphate group and the carboxylate group of the linker.[37,38] Bearing this in mind, we hypothesized that using functional molecules with carboxylic terminus to occupy the open coordination sites on the Zr_6 cluster can impede the attack of phosphate, thereby achieving the desired effect of sustained release. Folic acid (FA) is a carboxylate-containing organic compound that could readily bind to the vacant sites on Zr_6 clusters.[41–43] This interaction results in the formation of a stable complex that exhibits a sustained-release effect through steric hindrance when exposed to physiological conditions. More significantly, Gan et al. recently reported a unique intestinal pathological characteristic in diabetic animals where the expression of proton-coupled folate transporter (PCFT) in intestinal epithelial cells is upregulated at both mRNA and protein levels.[44] In light of this, FA-conjugated nMOFs could gain the capability to favorably alter the transcellular selection of materials (i.e., a conjugated drug delivery platform) through the upregulated transporters mediating endocytosis and thereby facilitating oral INS delivery, particularly in diabetic animals. Therefore, the conjugation of FA on nMOFs is not only expected to improve the intestinal penetration efficiency of MOF nanoplatforms for efficient oral delivery but also may function as a unique molecular tuning knob to finely tune the disintegration of MOFs in a phosphate-rich bloodstream environment to realize steady drug release, which is unprecedented in other types of organic or inorganic nanocarriers of INS.

In this contribution, we report the design of an oral sustained INS delivery platform based on functionalized FA-conjugated acid-resistant MOF (PCN-777) NPs (Scheme 1). The selection of PCN-777 is based primarily on the fact that it possesses one of the largest cage sizes (~3.8 nm) and the highest pore volume of 2.8 $cm^3\ g^{-1}$ among the reported Zr-MOFs,[45] allowing a considerable amount of INS to be encapsulated. PCN-777 also displays a high level of acid-aqueous solution stability despite its high porosity, which makes it an ideal protective carrier of INS. Furthermore, the coordination sites of the Zr_6 cluster in PCN-777 are partially occupied by six carboxylate organic linkers, leaving abundant positions to be occupied by terminal OH/H_2O groups,[45] which can be facilely substituted by FA under mild conditions so as to achieve sustained release and enhanced oral administration of INS. Moreover, according to the literature,[46] mucus contains negatively charged carbohydrate groups that can interact electrostatically with positively charged PCN-777 nanocarriers. The electrostatic interactions can enhance mucosal adhesion, prolong the retention time of NPs on the mucosal surface, and improve their intestinal absorption rate. Overall, the FA-conjugated PCN-777 holds promise as an ideal nanoplatform for oral protein delivery, distinguished not only by its remarkable protein protection and efficient intestinal permeation but also by the prolonged and controlled protein release within the physiological environment through a delicate design

Please cite this article in press as: Zou et al., Efficient oral insulin delivery with sustained release by folate-conjugated metal-organic framework nanoparticles, Matter (2024), https://doi.org/10.1016/j.matt.2024.101948

CellPress

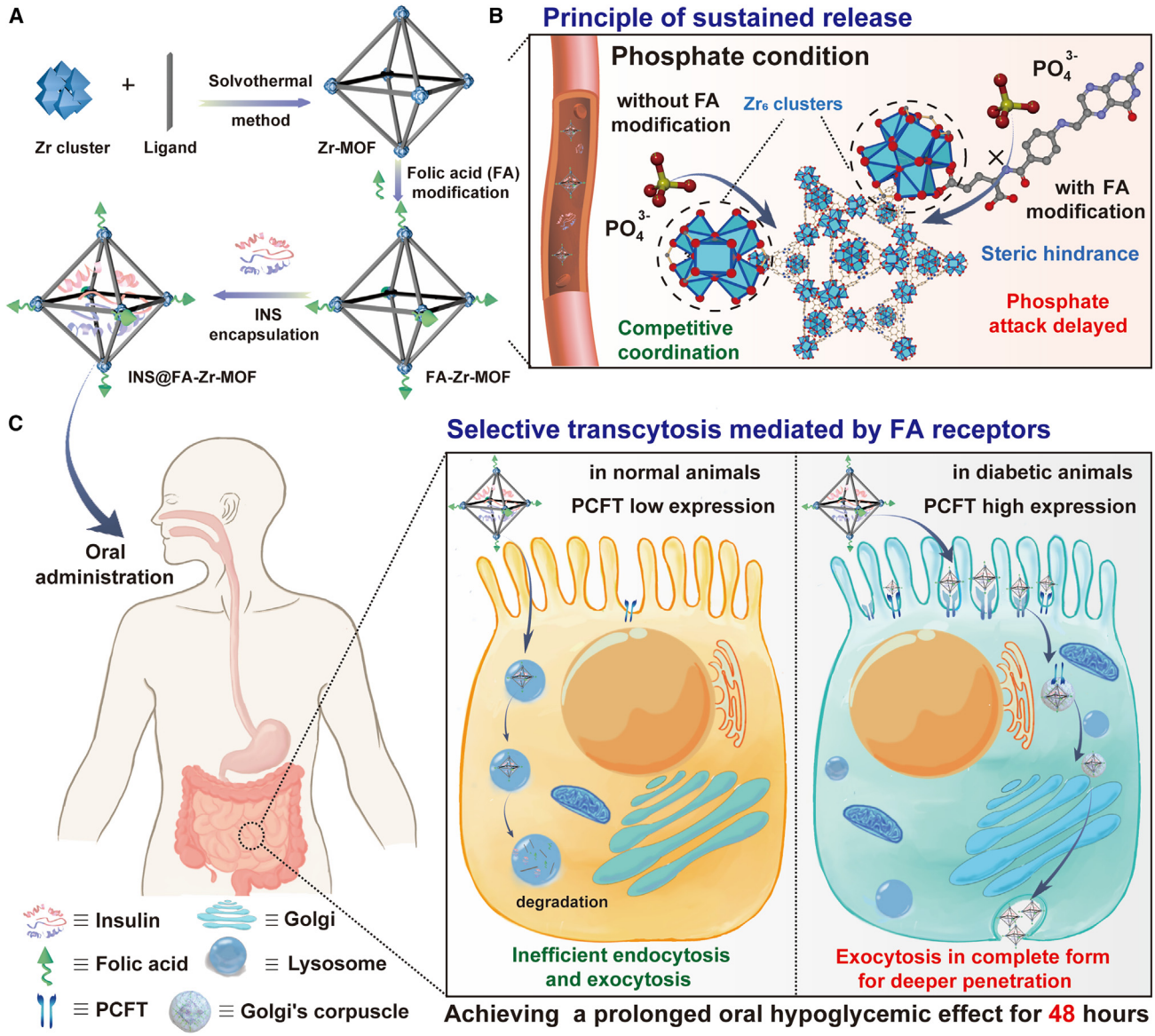

Scheme 1. Schematic representation of FA-modified Zr-based MOF for sustained oral delivery of INS

(A) The synthetic process of FA-modified Zr-based MOF delivery system.

(B) Schematic illustration of the sustained release mechanism of FA-modified Zr-based MOF.

(C) Schematic illustration of the selective endocytosis pathways of FA-modified Zr-MOF. In the presence of low expression of PCFT in normal animals, FA-modified Zr-MOF NPs were mainly internalized by a clathrin-mediated pathway and subsequently digested by lysosomes. In the case of the high expression of PCFT in diabetic animals, MOF NPs are endocytosed through the pathway mediated by caveolae and thus exocytosed in a complete form to achieve efficient transcellular transport efficiency.

of nanocarrier. Notably, the FA-conjugated PCN-777 would also exhibit a highly selective hypoglycemic effect exclusive to diabetic animals, which minimizes the risk of medication errors in non-diabetic individuals, thereby averting the unpredictable consequences of severe hypoglycemia. The combination of the aforementioned distinctive features would ultimately prolong drug action and enhance the bioavailability of INS after oral administration, accompanied by optimized pharmacokinetics (PK) and a potential reduction of hypoglycemia risk. This research advanced the concept that MOF can achieve effective and long-term oral protein delivery after proper modification, taking MOF-based drug delivery systems one step closer to clinical application.

RESULTS

Preparation and characterization of MOF-based sustained delivery nanosystems

The preparation procedures of PCN-777 NPs, FA-conjugated PCN-777 NPs (F-P NPs), INS-encapsulated PCN-777 NPs (I@P

Please cite this article in press as: Zou et al., Efficient oral insulin delivery with sustained release by folate-conjugated metal-organic framework nanoparticles, Matter (2024), https://doi.org/10.1016/j.matt.2024.101948

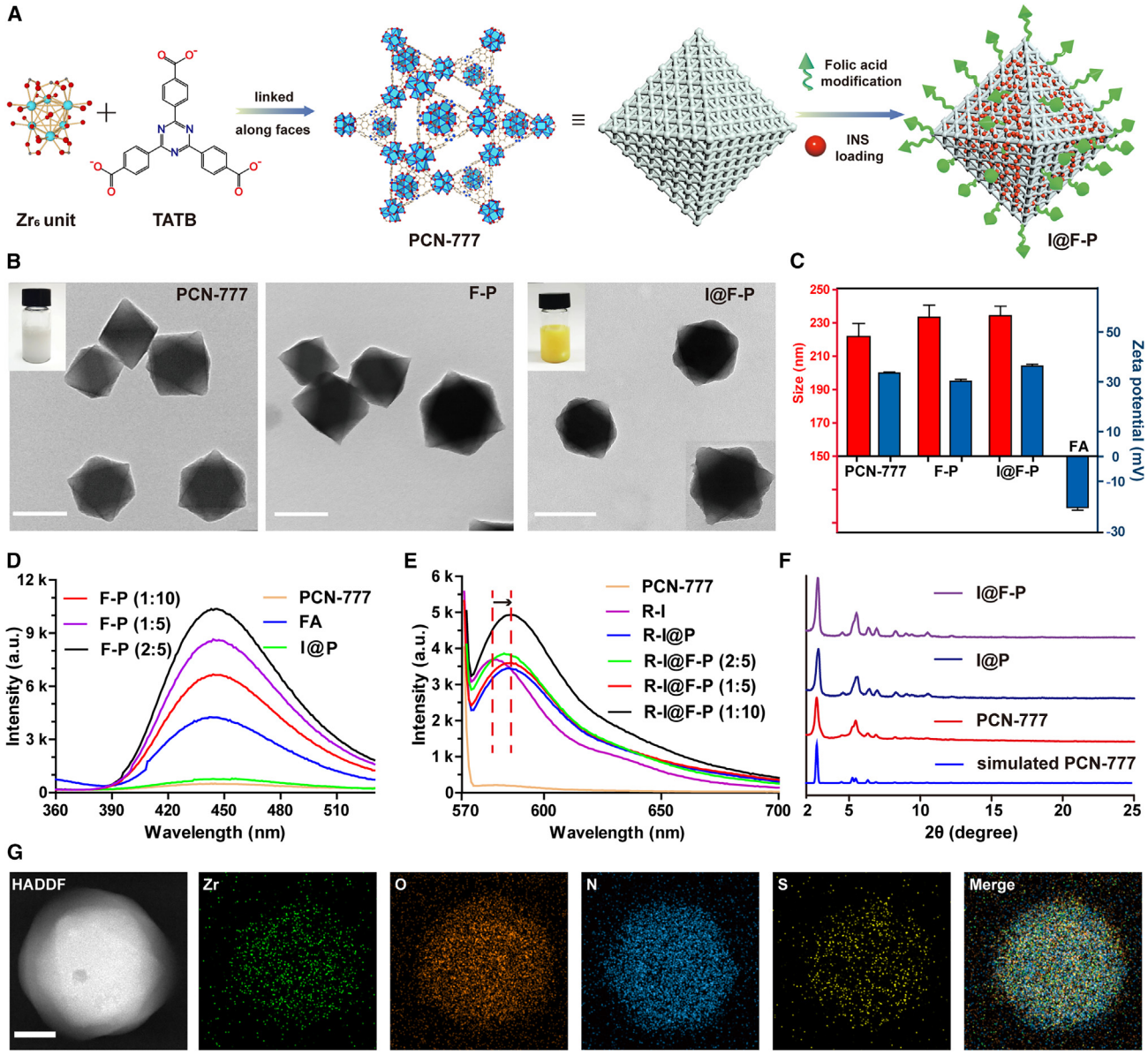

Figure 1. Preparation and characterizations of PCN-777-based nanosystems

(A) The synthetic protocol of the sustained-release MOF nanosystem. TATB, 4,4′,4″-*s*-triazine-2,4,6-triyl-tribenzoate.

(B) TEM images of PCN-777-based nanosystems. Scale bar, 200 nm.

(C) Size distributions and zeta potential of PCN-777-based nanosystems (n = 3 independent samples, mean ± SD).

(D) Emission spectra of different preparations with excitation at 280 nm.

(E) Emission spectra of different preparations with excitation at 560 nm. The INS concentrations for R-I, I@P, I@F-P (1:10), I@F-P (1:5), and I@F-P (2:5) are 272, 242, 254, 347, and 278 μg/mL, respectively.

(F) PXRD patterns of as-synthesized PCN-777-based nanosystems.

(G) The EDS elemental mapping analyses of I@F-P NPs. Scale bar, 50 nm.

NPs), and INS-encapsulated F-P NPs (I@F-P NPs) are presented in Figure 1A. In previous reports, the particle size of PCN-777 was commonly above 500 nm,[47–49] which is not conducive to crossing the intestinal barriers. Therefore, we synthesized the PCN-777 NPs with a particle size distribution of ∼220 nm through the optimized solvothermal method. Transmission electron microscopy (TEM) images and hydrodynamic diameters revealed that the PCN-777-based nanosystem was composed of homogeneous regular octahedrons (Figures 1B and 1C). Since FA is not soluble in water at room temperature, considering the instability of protein in organic solvents, we encapsulated INS after installing FA on PCN-777 during the stepwise synthetic processes. After FA modification and INS encapsulation, the color of the NPs turned yellow, the surface changed from smooth to

rough, and the particle size increased slightly. The PCN-777-based nanosystem also exhibited non-negligible zeta potential changes during the consecutive conjugation and encapsulation processes, initially decreasing from +33 to +30 mV due to the negative charge nature of FA, and subsequently increasing to +36 mV after INS loading (Figure 1C). Based on the observed changes in zeta potential, we inferred that INS binds to the MOF interior with minimal electrostatic interactions. Furthermore, considering that the PCN-777 nanocarrier possesses a significantly hydrophobic inner surface, the encapsulation of INS is predominantly facilitated by hydrophobic interactions. To further confirm the modification and immobilization of FA and rhodamine isothiocyanate (RITC)-labeled INS (R-I) in PCN-777 NPs, we next performed fluorescence spectroscopy and UV-visible (UV-vis) spectroscopy measurements. The fluorescence spectrum of F-P NPs showed the characteristic absorption peak of FA at ~450 nm (Figure 1D), illustrating the successful conjugation of FA. Likewise, the characteristic emission peak of R-I in RITC-INS@FA-PCN-777 (R-I@F-P NPs) was at ~580 nm in fluorescence spectrum, and the absorption peak at ~560 nm in UV-vis spectrum provided the expected evidence of INS encapsulation (Figures 1E and S1). Notably, the absorption peaks of R-I in the R-I@P NP and R-I@F-P NP groups were redshifted by 4–5 nm. This was attributed to the aggregation of R-I molecules in the PCN-777 NPs, providing further evidence that INS was entrapped in the PCN-777 NPs in large quantities rather than dispersed on the surface. The powder X-ray diffraction (PXRD) patterns of I@P NPs and I@F-P NPs were essentially identical to that of PCN-777 NPs (Figure 1F), indicating that PCN-777 NPs maintained good crystallinity during the processes of FA modification and INS encapsulation. The energy-dispersive spectroscopy (EDS) elemental mapping analysis reveals that the FA-modified PCN-777 is devoid of sulfur elements (Figure S2). Upon loading INS, the distribution of Zr, S, N, and O elements is uniform on the surface of I@F-P NPs (Figure 1G), proving the successful synthesis of nanosized PCN-777 and encapsulation of INS. In addition, the degree of FA functionalization has a crucial impact on the particle size, sustained release effect, and cellular uptake of NPs.[43] Therefore, we prepared and characterized a series of FA-modified PCN-777 NPs in different proportions (Figure S3). The loaded amount of FA on the surface of PCN-777 NPs was measured through the standard curves with a good linear relationship (Figure S4). As the feeding ratio of FA to PCN-777 increased from 1:10 to 2:5, the amount of surface-installed FA increased from 41 to 218 mg FA/g MOF. Additionally, before determining the INS LC of PCN-777, we employed the bicinchoninic acid (BCA) assay to measure the absorbance of the saturated FA solution and the MOF supernatant to eliminate potential interference from FA and residual metals on the protein determination (Figure S5). The results indicate that there is no significant difference in absorbance between the saturated FA solution, the MOF supernatant, and double-distilled H_2O (ddH_2O), suggesting that the BCA assay offers a high degree of accuracy in quantifying the INS loading and can be reliably used in subsequent experiments. We first evaluated the LC of PCN-777 for INS, which showed a considerable LC with a maximum of up to 121.6 wt % (INS:PCN-777) at a feeding ratio of 3:1. Following the modification of FA on PCN-777, the influence of F-P NPs with varying FA densities on the encapsulation of INS per gram of PCN-777 was found to be negligible (Figure 2A). This is likely due to the fact that FA mainly modifies PCN-777 by coordinating with Zr_6 clusters on the surface without occupying the pores.[45] In the final formulation of I@F-P NPs, the three components in the I@F-P NPs existed in the weight ratio of 50:41:9 (INS:PCN-777:FA), in which the loading content of INS was approximately 50 wt %, indicating that 2 mg I@F-P NPs can effectively deliver 1 mg INS. The thermogravimetric analysis (TGA) also verified the high loading content of INS by PCN-777 NPs (Figure S6).

In addition to the demand for high drug loading, clinical applications put forward stringent requirements for the uniformity and stability of nanomedicine. Therefore, we explored the stability of the PCN-777-based nanosystems under prolonged incubation time in solutions of ddH_2O or serum-containing medium by dynamic light scattering (DLS) analysis. As shown in Figure S7, no significant change in particle size in ddH_2O demonstrated the excellent stability of PCN-777-based nanosystems in aqueous environments, which also makes PCN-777 NPs an attractive candidate for the integration of multiple functions desired in oral protein delivery. Although we observed the particle size of I@F-P NPs slightly increasing up to ~300 nm in the complete DMEM, there was no significant difference between the nanoparticle sizes under prolonged incubation. These results proved that the PCN-777-based nanosystems would not aggregate in large quantities in the simulated *in vivo* environment and lead to potential dangers such as blood vessel blockage. We then investigated whether PCN-777 NPs have the ability to protect INS from protease degradation similar to our previously reported UiO-68-NH_2 NPs. As illustrated in Figure 2B, about 70% of the active INS remained in the I@F-P NPs group after 3 h of incubation with trypsin buffer, exhibiting a more profound protein protection ability than UiO-68-NH_2.[37] This phenomenon may be related to the better stability of PCN-777-based nanosystems in phosphate-containing buffers, as well as the denseness of INS inside PCN-777-based nanosystems. To further evaluate whether the structure and bioactivity of INS are retained during the encapsulation and release processes, we first analyzed the circular dichroism (CD) spectra of INS released from I@F-P. As can be seen in Figure S8, both free INS and INS released from I@F-P NPs exhibited distinct absorption peaks in the range of 200–220 nm, indicating that the secondary structure of the INS remains unchanged. Subsequently, we thoroughly disrupted the I@F-P NPs that had been stored for 2 months post-synthesis and subcutaneously injected the released INS into diabetic rats to further evaluate its bioactivity. As depicted in Figure 2C, the INS released by I@F-P NPs had a significant hypoglycemic effect on diabetic rats, similar to the equivalent dose of free INS, thereby demonstrating that the FA-modified PCN-777 nanosystem could effectively prevent drug performance loss during INS embedding, long-term storage, and release process. Overall, the PCN-777-based delivery system features high drug loading, high stability, and good protein protection, which facilitate the storage, transportation, and subsequent efficient oral delivery of protein drugs.

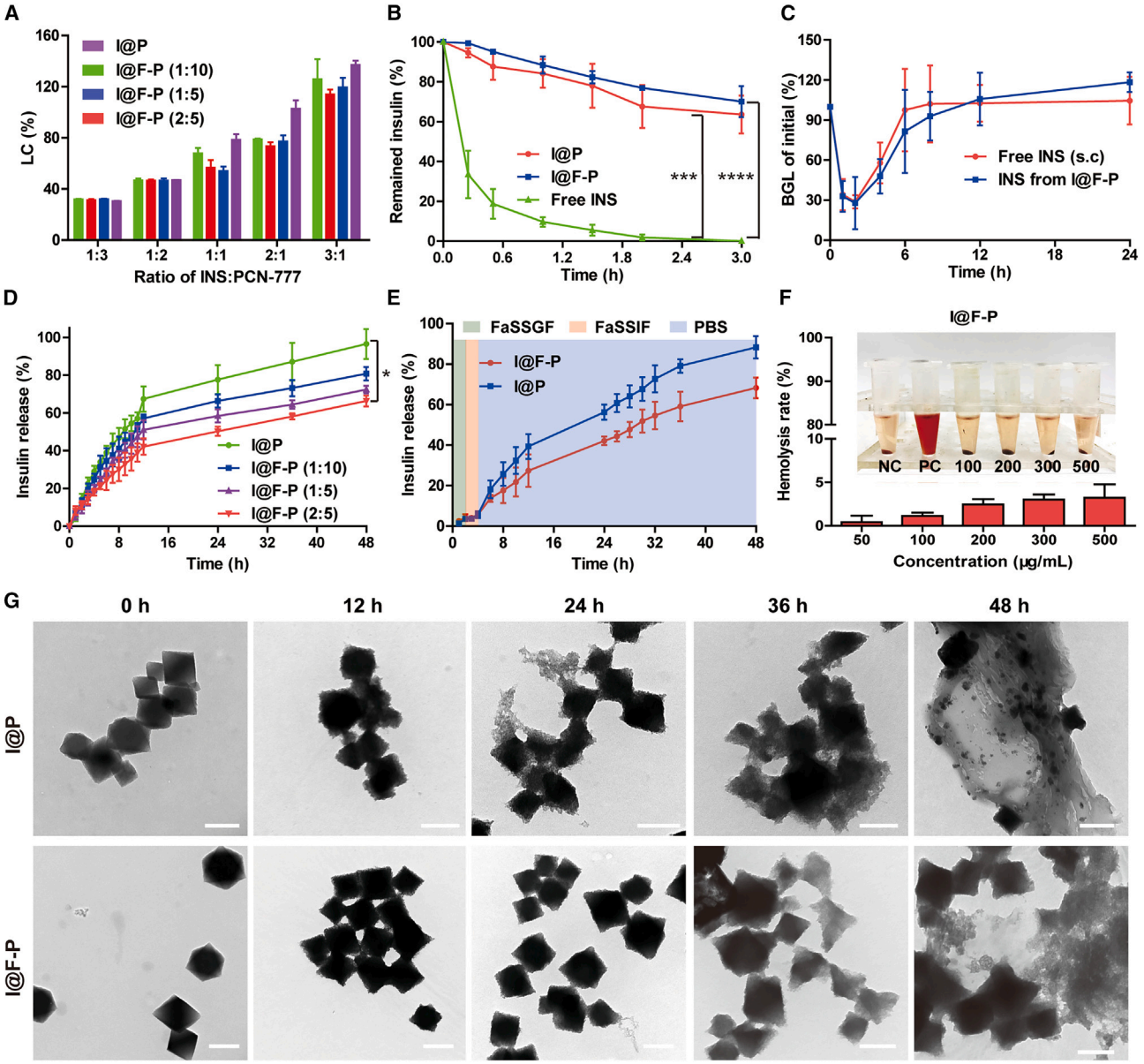

Figure 2. The *in vitro* release performance of the FA-modified PCN-777 nanosystem

(A) Comparison of the INS loading capacity of PCN-777-based nanosystems with different feeding ratios (n = 3 independent samples, mean ± SD).

(B) The enzymatic degradation profiles from different preparations after incubation with trypsin buffer at 37°C for various time points (n = 3 independent samples, mean ± SD).

(C) Blood glucose response of diabetic rats to free INS and INS released from I@F-P NPs (n = 3 biologically independent animals, mean ± SD).

(D) The *in vitro* release kinetics of I@P NPs and I@F-P NPs with different feeding ratios under phosphate conditions (n = 3 independent samples, mean ± SD).

(E) Continuous release of INS from I@P NPs and I@F-P NPs under different pH environments (n = 3 independent samples, mean ± SD).

(F) The hemolysis analysis of I@F-P NPs (n = 3 independent samples, mean ± SD). NC, negative control; PC, positive control.

(G) The changes in the morphology of I@P NPs and I@F-P NPs immersed in PBS for 48 h. Scale bar, 200 nm.

p values are denoted as follows: ns, no significance, *$p < 0.05$, **$p < 0.01$, ***$p < 0.001$, and ****$p < 0.0001$.

Sustained and controlled INS release kinetics of I@F-P NPs

Next, we tested the stability and release profile of the PCN-777-based nanosystems in different physiological conditions (Figures 2D and S9). It can be observed that the I@P NP group released less than 10% of INS in 8 h (<35% in 48 h) in both the simulated gastric fluid (FaSSGF) and simulated intestinal fluid (FaSSIF) environment, while the I@P NPs continuously and slowly released up to 93% of INS within 48 h in PBS. It is worth noting that the cumulative release of INS from the I@F-P NPs was

remarkably lower than that of the I@P NP group in 48 h, attributable to the higher PBS stability of FA-modified PCN-777. To further examine this phenomenon, we explored the release profiles of I@F-P NPs with different FA/PCN-777 feeding ratios under phosphate-containing conditions. As shown in Figure 2D, the cumulative release of INS from I@F-P NPs in the PBS environment was remarkably reduced with the increase in the amount of FA modification, and when the feeding ratio of FA to PCN-777 increased to 2:5, the cumulative INS release of I@F-P decreased to 67% within 48 h. We found that phosphate-triggered release was significantly mitigated by increasing amounts of FA modification due to the steric hindrance between FA and PCN-777 greatly impeding the attack of Zr_6 clusters from phosphate, thus creating a quite specific process leading to the delay in the decomposition time of PCN-777. In addition, we calculated the release characteristic index *n* value according to the Ritger-Peppas models.[50] The *n* values of all nanosystems (I@P NPs and I@F-P NPs with different modification densities of FA) were greater than 0.45 (Table S2), which proved that the INS release mechanism of PCN-777-based nanosystems was non-Fick diffusion (anomalous transport; i.e., the combined effect of drug diffusion and matrix erosion). To simulate the dissolution and release of orally administered drugs at multiple levels in different media of the GIT, we further explored the continuous INS release of I@P NPs and I@F-P NPs in FaSSGF, FaSSIF, and PBS environments. Consistent with the previous results, I@P NPs and I@F-P NPs barely released INS under acidic conditions. However, after being incubated in a neutral PBS environment, INS from I@P NPs and I@F-P NPs began to release slowly (Figure 2E). These results demonstrated that the PCN-777 nanocarrier was stable, with little INS release in the GIT, and disintegrated with a sustained rate under phosphate-containing conditions.

Subsequently, to intuitively reflect the protective effect of FA on PCN-777, we further monitored the morphological changes of I@P NPs and I@F-P NPs after incubation with PBS for different time intervals. As shown in Figure 2G, the I@F-P NPs became rough and started to decompose slowly, yet the regular octahedral morphology was well maintained for up to 24 h. It is worth noting that in the absence of FA modification, I@P NPs lose their basic morphology at 12 h and are fully cleaved at 48 h. This result is consistent with the release profile, which validates our conjecture that the conjugation of FA on Zr-based MOF can retard its disintegration in PBS and prolong the curative effect of the short half-lived proteins via sustained release. We also conducted scanning electron microscopy (SEM) and PXRD analyses to evaluate the disintegration of the crystalline morphology of PCN-777 nanosystems. The SEM images showed that the surface of the I@F-P NPs gradually became rough due to the formation of irregular pores, which eventually led to fragmentation within 48 h (Figure S10). PXRD analysis further verified that the crystallinity of I@F-P NPs was gradually lost under PBS incubation within 48 h (Figure S11).

Biocompatibility analysis of I@F-P NPs

Safety is the prerequisite for long-term medication in chronic diseases. We first assessed the safety of PCN-777-based nanosystems in blood *in vitro* using an acute hemolysis assay. The hemolysis rate was 4.1% when administrated at a concentration of 500 μg/mL (Figure 2F), demonstrating that the PCN-777-based nanosystem exerted little damage to cell membranes and intracytoplasmic proteins. At the cellular level, we performed MTT (3-[4,5-dimethylthiazol-2-yl]-2,5 diphenyl tetrazolium bromide) assays and live/dead cell imaging assays. As shown in Figure 3A, the PCN-777-based nanosystems showed low cytotoxicity in three different cell lines, and the cell viability was above 85% even when administered at a concentration of 500 μg/mL, which was consistent with the live/dead cell staining (Figure 3B). At the level of healthy and diabetic animal models, we conducted a comprehensive assessment of the potential long-term biosafety of PCN-777-based nanosystems, which involved a thorough examination of changes in blood parameters, biochemical markers, pro-inflammatory cytokines, and tissue morphology after consecutive oral administration. Our results indicated that except for uric acid (UA), there were no significant differences in routine blood analysis, biochemical indicators, or serum pro-inflammatory cytokines between the PCN-777-based nanosystem group and the control group, even after 1 month of treatment (Figures 3C and 3D; Table S3). Although significant differences in UA levels were observed among different groups, the UA levels in mice exhibited considerable variability, ranging from 0.1 to 760 μM, all of which fall within the normal physiological range as reported in the literature.[51] In addition, the major organs and intestines exhibited intact structure with no notable difference compared with the control group (Figure S12), thereby confirming the excellent biocompatibility of the nanosystem and its absence of adverse effects on the functions of the liver, kidney, and heart. Moreover, acute toxicity testing at the highest dose of 2,000 mg/kg revealed that all diabetic mice survived for over 14 days without significant changes in body weight (Figure S13), and the H&E staining images of the organs also revealed no evident inflammatory responses or injuries (Figure S14). The results of the acute toxicity test highlight that the PCN-777 nanosystem displayed no conspicuous adverse effects at the tested dosage, signifying considerable implications for the design of subsequent long-term toxicity tests. The above results indicated that prolonged and consistent dosing schedules appear relatively safe, supporting the continued long-term application of the PCN-777 nanosystem. Furthermore, challenges stemming from MOF metabolism and the enduring presence of metal constituents continue to confront the biomedical applications of MOFs. As such, we initiated an investigation aimed at elucidating the distribution and persistence of MOFs within organisms. Following a continuous 14-day administration regimen, an evaluation of metal constituents within internal organs revealed that Zr residuals were all below 0.1 identification percentage per gram, well within safety parameters (Figure S15).[52] This reaffirms the feasibility of expanding the utilization of MOFs for further advancements in biomedical applications.

PCFT-mediated endocytosis studies of I@F-P NPs

Human colon adenocarcinoma (Caco-2) cell lines with high expression of PCFT served as the primary drug transportation cell model to predict the efficiency of I@F-P NPs intestinal absorption.[53] According to the literature, myricetin can inhibit the expression of PCFT.[54] Thus, we assessed the changes in

Please cite this article in press as: Zou et al., Efficient oral insulin delivery with sustained release by folate-conjugated metal-organic framework nanoparticles, Matter (2024), https://doi.org/10.1016/j.matt.2024.101948

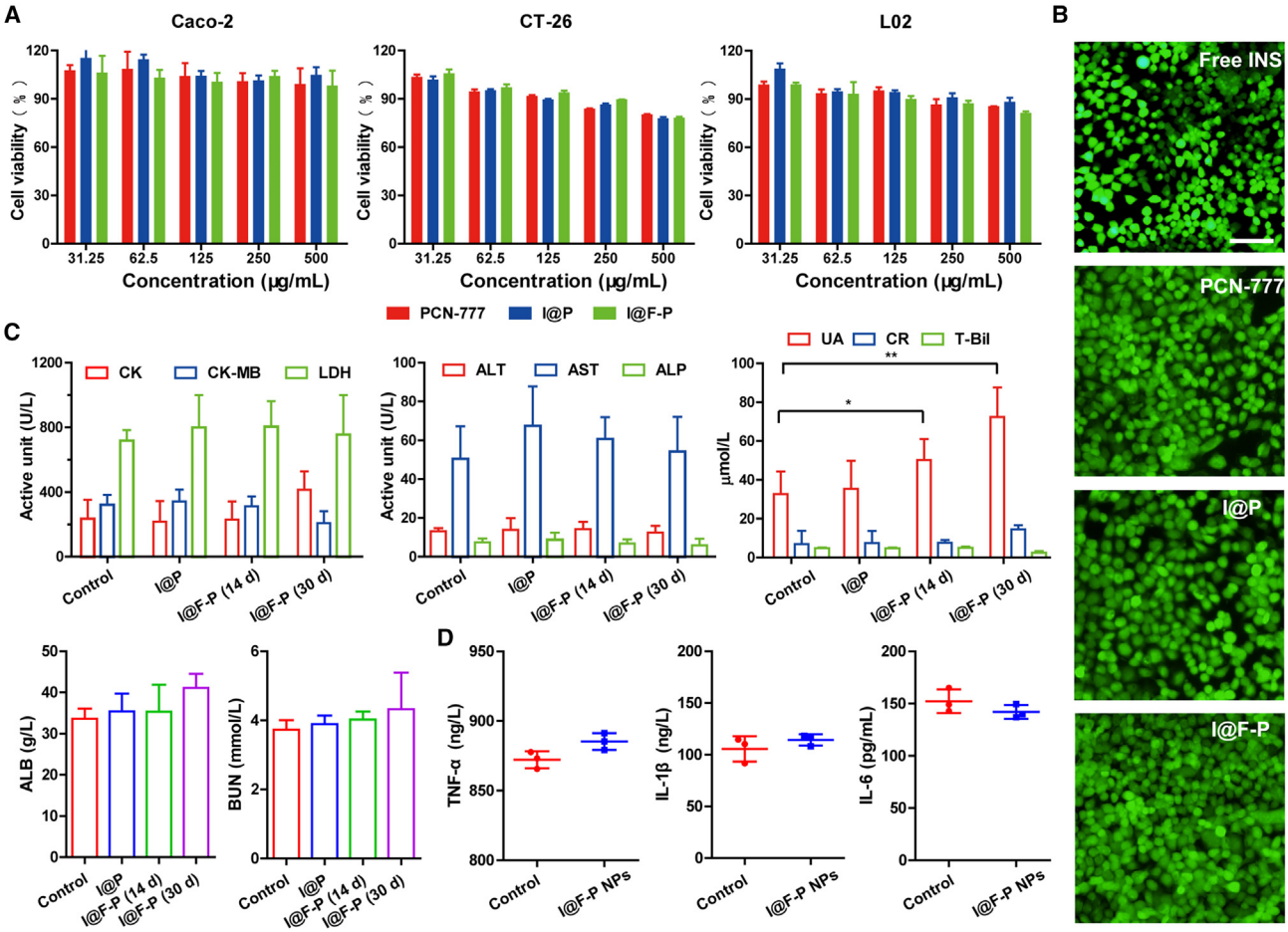

Figure 3. Biocompatibility of PCN-777-based nanosystems

(A) The *in vitro* cell viability test of PCN-777-based nanosystems for Caco-2 cells, CT-26 cells, and LO2 cells (n = 5 biological independent samples, mean ± SD).

(B) The live/dead imaging of PCN-777-based nanosystems. Scale bar, 100 μm.

(C) Analysis of blood biochemical indicators 2 weeks after PCN-777-based nanosystem administration (n = 5 biologically independent animals, mean ± SD). There are no significant differences among the three groups. ALB, albumin; ALT, alanine aminotransferase; ALP, alkaline phosphatase; AST, aspartate aminotransferase; BUN, blood urea nitrogen; CK, creatine kinase; CK-MB, creatine kinase isoenzyme; CR, creatinine; LDH, lactate dehydrogenase; T-bil, total bilirubin; UA, uric acid.

(D) Levels of pro-inflammatory cytokines in mouse serum following oral administration (n = 3 biologically independent animals, mean ± SD).

p values are denoted as follows: ns, no significance, *$p < 0.05$, **$p < 0.01$, ***$p < 0.001$, and ****$p < 0.0001$.

PCFT expression in Caco-2 cells following myricetin intervention via western blot analysis. The results demonstrated that myricetin significantly reduced PCFT expression in these cells (Figure S16). Therefore, Caco-2 cells with inhibition of PCFT expression by myricetin were used as the control group to investigate the effect of PCFT expression level on the endocytosis of I@F-P NPs in subsequent experiments. The qualitative and quantitative uptakes of PCN-777-based NPs in Caco-2 cell monolayers were visualized by laser confocal fluorescence microscopy (CLSM) and flow cytometry analysis (Figures 4A and S17–S19). The I@F-P NPs exhibited increased and time-dependent cellular internalization compared to other groups. In addition, the transportation depth of I@F-P NPs in the Caco-2 cell monolayer was closer to the basal side as evident from the red fluorescence distribution of the z axis (Figures 4A and 4B). According to the quantitative results obtained by flow cytometry, the cell uptake of I@F-P NPs is 9.9- and 2.1-fold that of free INS and I@P NPs groups, respectively. Notably, the I@F-P NP internalization in PCFT-expressing suppressed cells was comparable to that of the I@P NP group and the internalization of I@F-P NPs gradually rose with the increasing FA density, which confirmed that the cellular internalization of the I@P NPs group was mediated by the PCFT pathway.

To further investigate the endocytosis mechanisms of the I@F-P NPs, we used different endocytosis inhibitors while co-incubating the cells with I@F-P NPs following the protocol previously reported in the literature.[44,55] As shown in Figures 4C, 4D, and S20, the cellular internalization of I@F-P NPs decreased dramatically at 4°C in both high- and low-expression cell lines, suggesting that the cellular uptake of I@F-P NPs was energy dependent. The use of filipin and methyl-β-cyclodextrin/lovastatin could inhibit caveolin-mediated

Please cite this article in press as: Zou et al., Efficient oral insulin delivery with sustained release by folate-conjugated metal-organic framework nanoparticles, Matter (2024), https://doi.org/10.1016/j.matt.2024.101948

CellPress

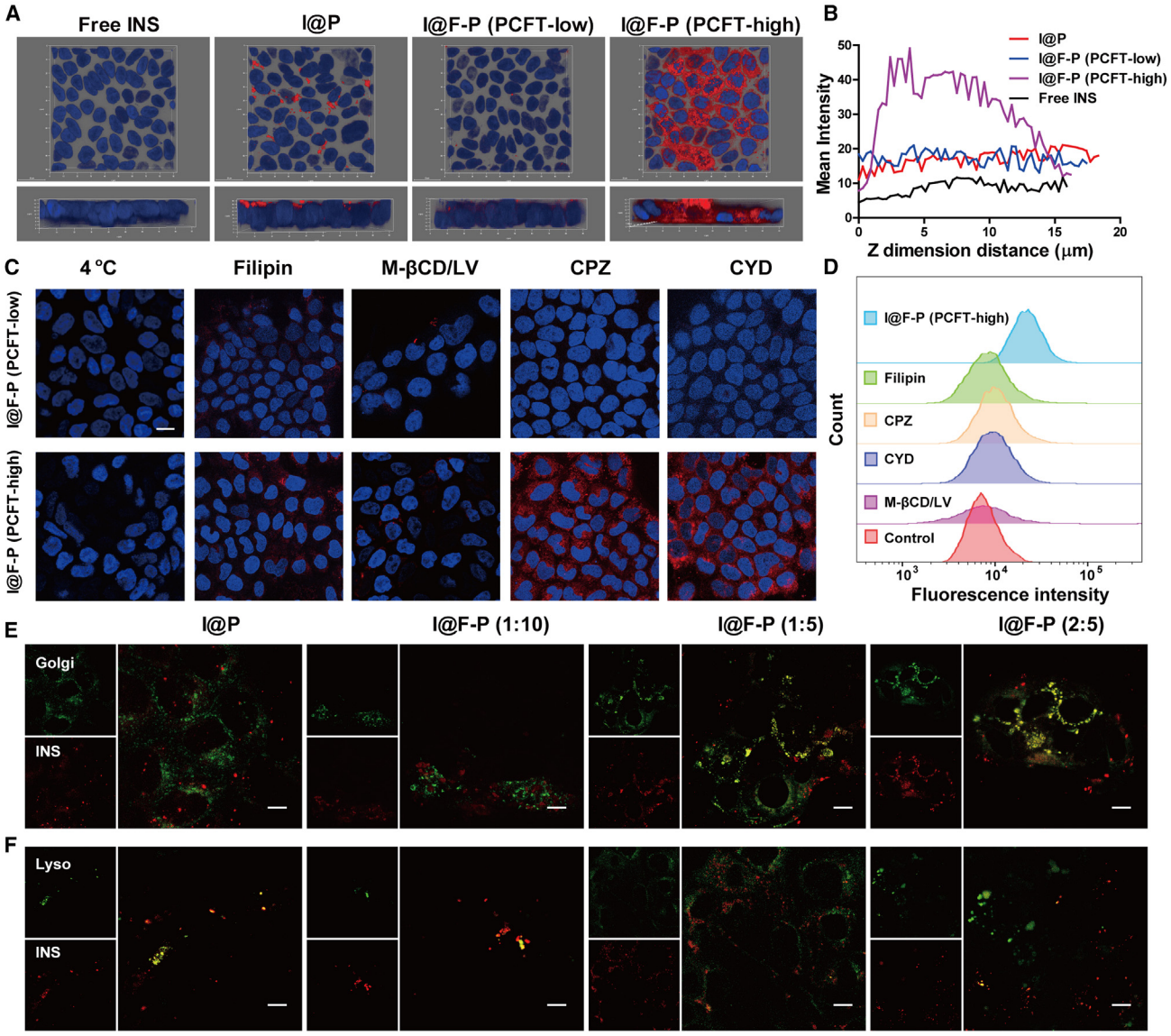

Figure 4. PCFT-mediated selective endocytosis of I@F-P NPs

(A and B) CLSM three-dimensional images and fluorescence quantitative analysis of RITC-labeled INS, I@P NPs, and I@F-P NPs incubated with Caco-2 cell monolayers exhibiting varying PCFT expression levels for 4 hours. Blue represents the nuclei and red represents the RITC-labeled INS preparations. Scale bar, 20 μm.

(C) CLSM images of the endocytosis mechanisms of I@F-P NPs (red) in Caco-2 cells (blue) pretreated with different inhibitors. Scale bar, 15 μm. CPZ, chlorpromazine; CYD, cytochalasin D; LV, lovastatin; M-βCD, methyl-β-cyclodextrin.

(D) Quantitative determination of I@F-P NPs cellular uptake amounts for different inhibitor treatments at 4 h.

(E) The co-localization images of Golgi (green) and I@F-P NPs (red) with different feeding ratios of FA:PCN-777 at 4 h. Scale bar, 10 μm.

(F) The co-localization images of the lysosome (green) and I@F-P NPs (red) with different feeding ratios at 4 h. Scale bar, 10 μm.

endocytosis by binding to cell membrane cholesterol and non-selectively depleting cholesterol. The cellular internalization of I@F-P NPs was reduced to 55% upon the addition of filipin and to about 42% when co-incubated with methyl-β-cyclodextrin and lovastatin, demonstrating that the caveolin pathway plays a significant role in the cellular internalization of I@F-P NPs. The addition of chlorpromazine suppressed the clathrin-mediated endocytosis, and the absorption of I@F-P NPs was reduced to 76% by chlorpromazine. This suggests that the clathrin pathway is also partly involved in the cellular uptake of I@F-P NPs. The cellular internalization of I@F-P NPs was slightly reduced after adding cytochalasin D for the inhibition of micropinocytosis. The above results were consistent with previous reports that caveolae-mediated endocytosis dominates the cellular uptake of FA-modified NPs, which may be related to the upregulated folate transporter.[44] The

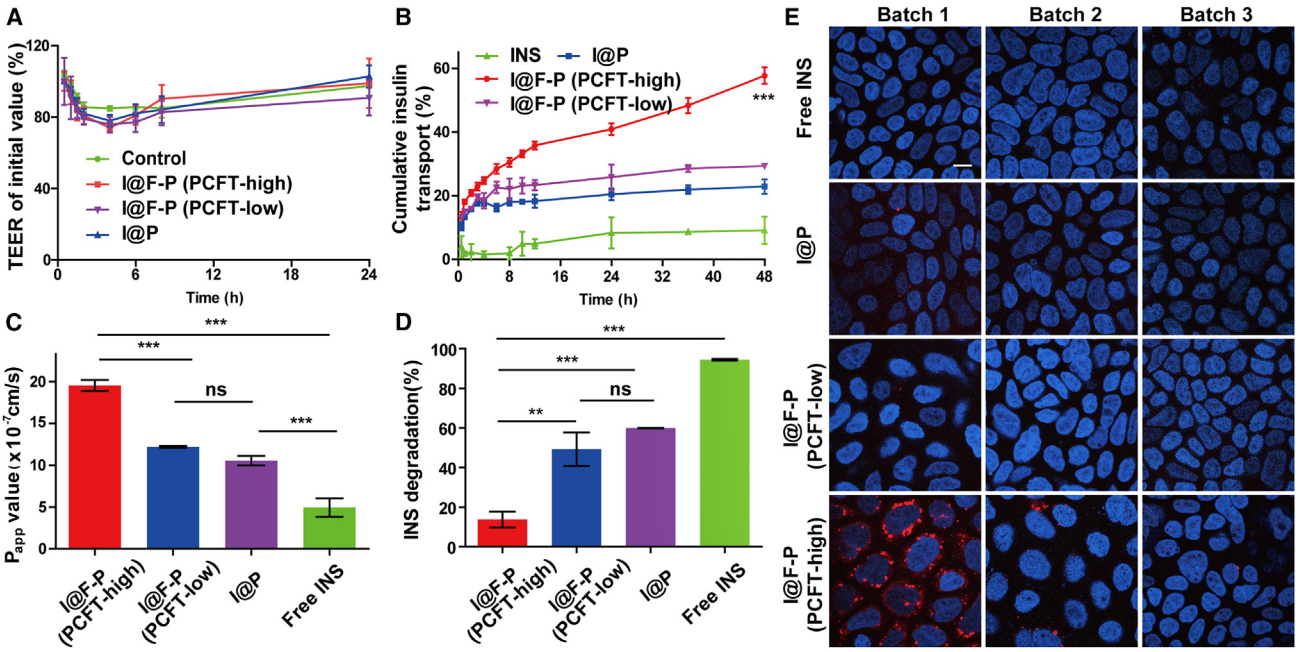

Figure 5. Transmembrane transport of I@F-P NPs in the high-expression and low-expression PCFT Caco-2 cell monolayer model

(A) Effects of different formulations on TEER of Caco-2 cell monolayers (n = 3 biologically independent samples, mean ± SD).

(B and C) The cumulative transportation and apparent permeability coefficient (Papp) of INS from different formulations across the Caco-2 cell monolayer in 48 h (n = 3 biologically independent samples, mean ± SD).

(D) Lysosomal degradation of INS from different formulations measured after incubating the cell monolayers for 48 h (n = 3 biologically independent samples, mean ± SD).

(E) Intracellular transfer of different INS formulations in three different cell batches visualized by CLSM. Scale bar, 10 μm.

p values are denoted as follows: ns, no significance, $^{*}p < 0.05$, $^{**}p < 0.01$, $^{***}p < 0.001$, and $^{****}p < 0.0001$.

clathrin-mediated endocytosis and micropinocytosis were also partially involved in the entry process of I@F-P NPs, but to a lesser extent. In contrast, the cellular uptake of I@F-P in the low-expression group was mainly through the clathrin-mediated pathway, which may explain the greatly reduced uptake after inhibiting the PCFT. The above results demonstrated that upregulated PCFT alters the transcellular pathway of I@F-P NPs from clathrin-dominated to caveolin-dominated endocytosis.

Subsequently, we performed intracellular localization experiments of PCN-777-based nanosystems to further confirm that upregulated PCFT mediates transcellular transport. In previous literature reports, NPs are transported to lysosomes after clathrin-mediated endocytosis, leading to degradation, whereas NPs are transported to the Golgi apparatus after caveolin-mediated endocytosis and subsequently exocytosis in the intact form.[56–58] As depicted in Figures 4E, 4F, and S21, almost all fluorescence signals of I@P NPs were co-localized with the lysosome rather than the Golgi. When the amounts of modified FA on the surface of the nanosystem increased, the co-localized organelles of I@F-P NPs gradually changed from the lysosome to the Golgi. We quantitatively evaluated the co-localization efficiency of PCN-777-based nanosystems with lysosomes and the Golgi apparatus by measuring the co-localization rate and Pearson's correlation coefficient. As the amount of FA modification increased, the co-localization rate of the PCN-777 nanosystems with the Golgi apparatus significantly rose from 27.5% to 81.1%, while the co-localization rate with the lysosome decreased markedly. The Pearson correlation coefficient further indicated a strong correlation between the I@F-P NPs (2:5) and the Golgi apparatus. Thus, we concluded that I@F-P NPs could be internalized through the PCFT-mediated pathway in Caco-2 cells with the upregulated PCFT and further transported through the Golgi pathway.

To verify whether I@P NPs can efficiently undergo exocytosis through the Golgi pathway, we investigated the transcellular permeability of PCN-777-based nanosystems in Caco-2 cell monolayers afterward. We first examined the transepithelial electrical resistance (TEER) values of Caco-2 cell monolayers during PCN-777-based nanosystems treatment. No significant decrease in TEER was observed compared to the control group, confirming the integrity of the tight junction (Figure 5A). The cumulative penetration INS of I@F-P NPs in high PCFT expression cells reached 62% at 48 h, which was 2.1-, 2.7-, and 6.8-fold compared to I@P NPs, free INS, and I@F-P NPs in low PCFT expression cells, respectively (Figure 5B). As shown in Figure S22B, the fluorescence distribution of the INS preparations in the apical and basal cell layers was consistent with the above results. The apparent permeability coefficient (Papp) of I@F-P NPs across high PCFT expression Caco-2 monolayers was 20.6 × 10^{-7} cm/s (Figure 5C), showing that the permeability of I@F-P NPs was

Please cite this article in press as: Zou et al., Efficient oral insulin delivery with sustained release by folate-conjugated metal-organic framework nanoparticles, Matter (2024), https://doi.org/10.1016/j.matt.2024.101948

CellPress

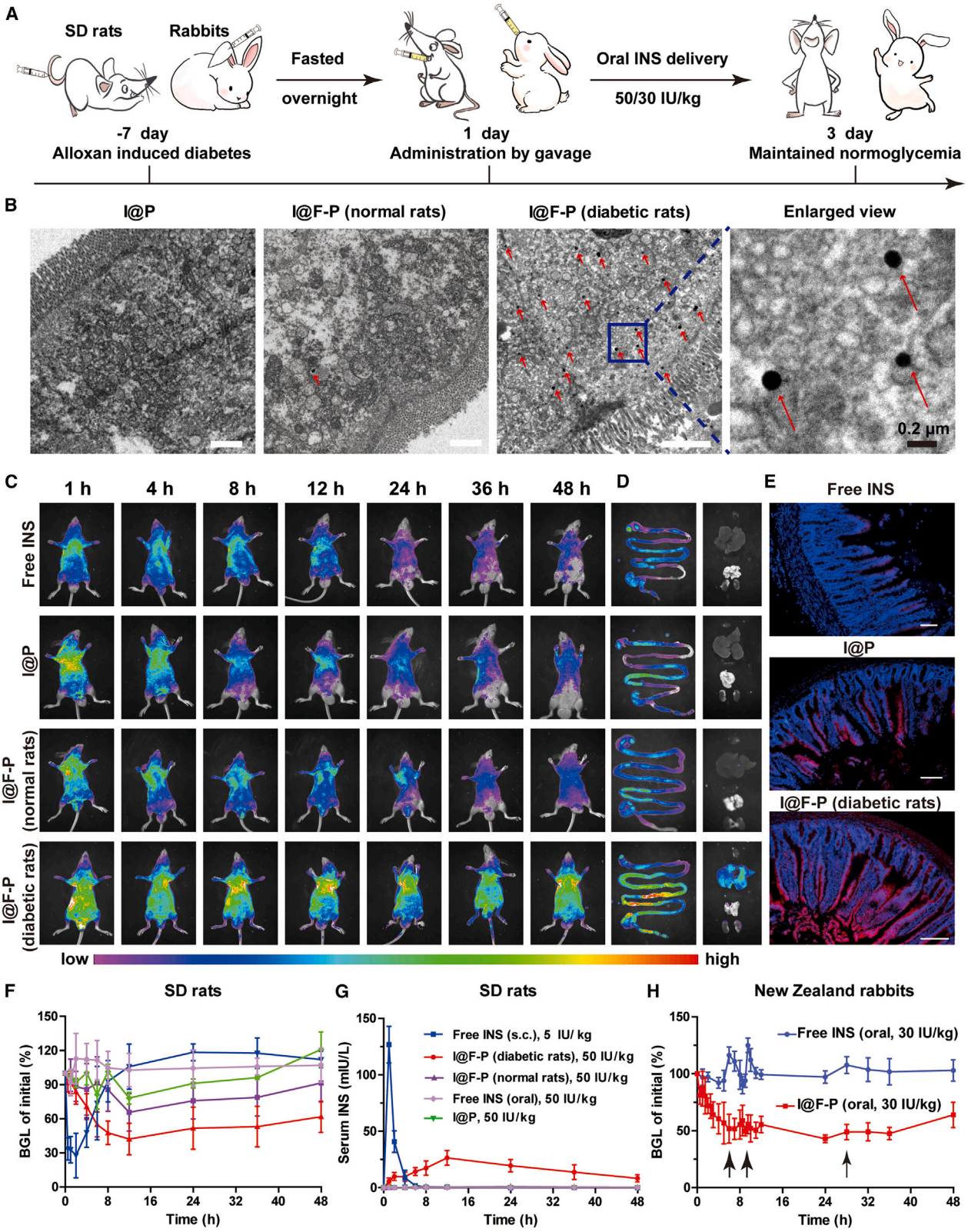

(legend on next page)

significantly improved in the high-expression group. Next, we took the culture medium on the basal side at 24 h, centrifugated it, and processed the precipitate for TEM. It can be seen in the corresponding figure (Figure S22C) that in the PCFT high-expression group, the I@F-P NPs maintained their complete morphological structure, while in the PCFT low-expression group, the octahedral shape of the I@F-P NPs could not be observed, which may be attributed to its destruction in lysosome through clathrin-mediated endocytosis. Following this, we calculated the INS degradation rate of different preparations in the Caco-2 cell monolayers as reported in the literature.[59] As shown in Figure 5D, the ingested INS in the free INS group almost completely degraded after 48 h of incubation, while the I@P NPs and I@F-P NPs groups significantly inhibited the degradation rate of INS in PCFT high-/low-expression cells. Compared with the I@P NPs group, the FA slightly hindered the lysosome degradation and reduced the degradation rate from 60% to 48% in the PCFT low-expression cells. In contrast, only about 15% of INS degraded in PCFT high-expression cells, which was attributed not only to the protection of F-P NPs but also to the internalization of I@F-P NPs through the Golgi-mediated pathway, avoiding endocytosis by lysosomes and reducing INS degradation. In addition to these tests, we conducted the transcellular transport of I@F-P NPs among different batches of cells using a previously reported protocol.[60] This investigation evaluated the ability of I@F-P NPs to undergo continuous endocytosis following endocytosis and exocytosis through fluorescence transfer between distinct cell batches, thereby verifying their transport efficiency across multiple cell layers. As illustrated in Figure 5E, the INS signal of I@F-P NPs in PCFT high-expressing cells remains relatively high in batches (2) and (3). This phenomenon indicated that I@F-P NPs absorbed by the cells in coverslip (1) were exocytotically released into the culture medium and subsequently internalized by cells on coverslips (2) and (3), demonstrating efficient transcellular transport via PCFT-mediated endocytosis. In contrast, the transport of I@P and I@F-P between PCFT low-expressing cells on coverslips (2) and (3) is notably limited. The above experiments proved that FA modification can increase the cellular uptake of I@F-P NPs through the PCFT-mediated pathway in high-expressing cells, avoiding the degradation of lysosomal uptake and thereby promoting the transcellular transportation of INS.

In vivo biodistribution and intestinal absorption

The excellent transportation outcomes of I@F-P NPs at the cellular level prompted us to validate their efficacy in diabetic small animal models. It is imperative to confirm the heightened expression of intestinal receptors in small animal models. Gan and colleagues's research has revealed substantial upregulation of the PCFT receptor within the GIT of rats.[44] In pursuit of broader validation, we extended our investigation to assess PCFT receptor expression in mice. Utilizing western blot experiments, we observed a notably elevated expression of PCFT in the duodenum, jejunum, and ileum of diabetic mouse models compared to the control group (Figures S23A and S23B). Additionally, the immunofluorescence staining has clearly delineated its predominant localization within the small intestinal villi (Figure S23C), a feature that confers significant advantages for facilitating intracellular drug delivery. As a result, we have substantiated that the expression of PCFT in the small intestine of diabetic animals consistently surpasses that in their non-diabetic animals, thus laying robust groundwork for our subsequent experiments.

Subsequently, we mapped the spatiotemporal distribution of the PCN-777-based nanosystem as it entered and exited the living body in detail using TEM, the Maestro *In Vivo* Imaging System, and CLSM to intuitively investigate the potential pathway and distribution of PCN-777-based nanosystems across the epithelial layer. Rats were sacrificed 4 h after gavage, and the small intestine was taken for TEM imaging (Figure 6B). Only I@F-P NPs were localized in epithelial cells in large quantities, showing that PCFT-mediated endocytosis enhanced the penetration efficiency of I@F-P NPs into intestinal epithelium. Subsequently, we obtained the *in vivo* images displaying the distribution of free INS, I@P NPs, and I@F-P NPs in normal mice and diabetic mice within 48 h. The results showed that a strong and persistent fluorescent signal up to 48 h was observed in the I@F-P NPs-treated diabetic mice, while the fluorescent signal in other groups was weaker and continued to decrease within 48 h (Figure 6C), providing solid evidence for the efficient intestinal transportation and long-term efficacy of I@F-P NPs in diabetic mice. It is worth noting that the observed fluorescence signal of I@F-P NPs in normal mice was nearly the same as that of the I@P NPs group, indicating that the expression level of PCFT in normal mice was relatively low, thus leading to ineffective drug absorption.

Figure 6. Enhanced and prolonged hypoglycemic effect validation of FA-modified PCN-777 nanosystem in animals

(A) Oral administration of the FA-modified PCN-777 nanosystems to the animals.

(B) TEM image of epithelial tissues collected 4 h after the oral administration of PCN-777-based nanosystems. The red arrow points to I@F-P NPs entering the intestinal tissue. Scale bar, 2 μm.

(C) Fluorescence distribution and intensity of the R-I *in vivo* at different time intervals after the oral INS administration from different formulations.

(D) *Ex vivo* fluorescence images of the intestine, and images of the heart, liver, spleen, lung, and kidney (from top to bottom) of the mice after the oral INS administration for 12 h.

(E) Images of sectioned intestine tissues of rats after oral administration of different R-I formulations for 12 h. Scale bar, 200 μm.

(F) Blood glucose levels of initial vs. time profiles of the diabetic and normal Sprague-Dawley rats following the oral administration of I@F-P NPs, I@P NPs, and free INS, as well as subcutaneous (s.c.) injection of free INS (n = 5 biologically independent animals, mean ± SD).

(G) The serum INS levels vs. time profiles of the diabetic and normal Sprague-Dawley rats following the same formulations in (F) (n = 5 biologically independent animals, mean ± SD); details are shown in Figure S24.

(H) Time course profiles of blood glucose levels of the diabetic New Zealand rabbits following the oral administration of I@F-P NPs and free INS (n = 3 biologically independent animals, mean ± SD). The rabbits were fed at the time points marked by black arrows, 12 and 36 h.

Next, we investigated the biodistribution of INS in intestines and major organs after 12 h of administration (Figure 6D). A strong fluorescent signal was detected only in the intestinal tracts and livers of the I@F-P NPs group, demonstrating that only I@F-P NPs were efficiently absorbed by the intestinal tract and transported to the liver. Since the improved absorption of I@F-P NPs to diabetic mice was confirmed, we further monitored the uptake of I@F-P NPs in epithelial tissues of the intestine after 12 h of administration to observe its distribution in the intestine more intuitively (Figure 6E). The fluorescent signals observed were localized within intestinal epithelial cells and muscular layer, thus confirming that INS from I@F-P NPs had been successfully delivered into the intestinal villus, whereas only weak fluorescence between the intestinal villi gaps was observed in the free INS and I@P NPs groups. The above results indicated that I@F-P NPs have a satisfactory selective long-acting oral delivery function for diabetic mice.

In vivo pharmacodynamics and PK studies

Finally, we investigated the hypoglycemic response and PK effects of PCN-777-based nanosystems in fasted diabetic rats by gavage. As shown in Figure 6F, oral administration of free INS and I@P NPs to diabetic rats and oral administration of I@F-P NPs to normal rats all failed to generate a significant glucose response, whereas subcutaneous injection of INS and intragastric administration of I@F-P NPs produced a rapid hypoglycemic response in diabetic rats. Notably, the group with subcutaneous injection of INS quickly restored high BGLs within 4 h, while the I@F-P NPs group achieved the best hypoglycemic effect (BGL down to 45%) at 12 h and maintained for 48 h. The pharmacological bioavailability of I@F-P NPs was about 38% based on the area above the curve of the profile in Figure 6F. The corresponding serum INS profiles of rats treated with different formulations were depicted as the area under the curve ($AUC_{0–48\ h}$) in Figures 6G and S24, which align with the pharmacodynamic outcomes. The calculated AUC of I@F-P NPs was 782.3 ± 126.3 mIU * h/mL with a relative bioavailability of 35.5% (Table S4). Notably, the sustained-release I@F-P NPs not only considerably improved oral INS utilization efficiency but it also exhibited a smooth time-effect curve for serum INS concentration, enabling better maintenance of INS concentration in rats within a narrow therapeutic range. Within this window, the BGL in rats was stably controlled for up to 48 h, reducing the incidence of side effects such as transient hypoglycemia. These results confirmed that I@F-P NPs significantly enhanced the oral delivery efficiency of INS in diabetic rats, demonstrated ultra-high oral bioavailability of INS, and provided a gentle and long-lasting hypoglycemic function.

To further verify whether I@F-P NPs can achieve similar glycemic control effects in different animal species, we also conducted oral I@F-P NPs administration verification on New Zealand rabbits. We administered I@F-P NPs intragastrically to fasting diabetic New Zealand rabbits with a medium dose (30 IU/kg) and measured their BGL in real time. As depicted in Figure 6H, the BGL was successfully reduced and maintained at normal levels for 48 h, even when rabbits were fed multiple times over different periods. In summary, I@F-P NPs could exert an extraordinary and long-lasting hypoglycemic effect on multiple diabetic species (mice, rats, and rabbits), thus providing new evidence and implications for subsequent pre-clinical studies on large animals.

DISCUSSION

Existing oral delivery methods for proteins/peptides with short half-lives suffer from cumbersome barriers that negatively affect their bioavailability and sustained release. Finding a feasible solution to these issues is extremely difficult and requires the development of a nanosystem that can effectively balance both needs for efficient delivery and long-term action. Building upon our prior research on acid-resistant MOFs that enabled successful oral delivery of INS, we constructed a new-generation nanosystem based on FA-functionalized Zr-based MOFs (PCN-777). By specifically coordinating functional molecules (FA) on the Zr_6 cluster of PCN-777, this nanosystem offers superior protein protection (kept 70% of INS active in trypsin buffer for 3 h), higher drug loading (up to 50 wt %), extended-release dosing (of up to 48 h), coupled with the ability to traverse the complex physiological barriers present and higher drug bioavailability. The final INS-loaded nanosystem (I@F-P NPs) showed they could be selectively and effectively absorbed by diabetic animals through the PCFT-mediated endocytic pathway. I@F-P NPs underwent efficient exocytosis through the Golgi pathway and maintained their octahedral shape in complete form during internalization for deeper penetration. Conversely, the I@F-P NPs were endocytosed in low efficiency through the clathrin-mediated pathway and became localized in the lysosome in normal animals with low expression of PCFT. The aforementioned advantages of the FA-conjugated PCN-777 nanosystem contributed to an oral INS bioavailability as high as 35.5% in diabetic rats. Moreover, we obtained a similar hypoglycemic effect maintained for 48 h in the diabetic New Zealand rabbit model. Meanwhile, no tissue lesions and abnormal biochemical indicators were observed in our safety experiments after multiple administrations. This work indicates that the implementation of the FA-conjugated PCN-777 nanoplatform with its sustained-release capability will significantly improve patient compliance by reducing INS dosing frequency, eliminating the need for constant injections, providing consistency in drug release over the long term, maximizing drug utilization, and ameliorating medication safety. This study also acknowledges several limitations. The identification of a distinct intestinal pathological feature in the human intestine has yet to be confirmed. Furthermore, it remains to be investigated whether different severities of diabetes induce varying changes in PCFT expression and whether these changes are consistent across different regions of the intestine. Our future studies would focus on these aspects, exploiting the variability in receptor expression between individuals and across different intestinal regions to design novel targeted or patient-customized MOF nanocarriers for oral protein delivery, opening up new possibilities for subsequent transformation toward clinical utilization.

METHODS

Materials

All standard synthesis reagents were purchased from commercial suppliers and used without any further purification. $ZrOCl_2 \cdot 8H_2O$, 4,4′,4″-*s*-triazine-2,4,6-triyl-tribenzoate (TATB), FA, and RITC were obtained from Energy Chemical. INS, DAPI, lysosome tracker, Golgi tracker, and the BCA kit were obtained from Bio-sharp. MTT and DMEM were purchased from Wuhan Kerui Biotechnology. The ELISA kits of bovine INS, interleukin-6 (IL-6), IL-1β, and tumor necrosis factor α (TNF-α) were obtained from Jiangsu Meimian Industrial Company. The PCFT (HCP1) rabbit monoclonal antibody and goat anti-rabbit immunoglobulin G (IgG)-horseradish peroxidase (HRP) were purchased from Beijing Bioss Biotechnology.

Preparation and characterization of PCN-777 NPs, I@P NPs, and I@F-P NPs

PCN-777 was synthesized through the solvothermal method according to the modifying methods reported in the literature. In brief, $ZrOCl_2 \cdot 8H_2O$ (52 mg), TATB (13 mg), and trifluoroacetic acid (0.24 mL) in dimethylformamide (DMF; 5 mL) were ultrasonically dissolved in a 20-mL Pyrex vial. The mixture was kept stirred at 120°C for 0.5 h. After cooling to room temperature, PCN-777 NPs were collected by centrifuging the mixture and washing it three times with DMF and methanol, respectively. A 200-μL solution was dried to a powder and weighed for quantification. For the preparation of F-P, 1 mL FA solution (2 mg/mL in DMF) was added to 5 mL PCN-777 (2 mg/mL in DMF) and vigorously stirred for 12 h in the dark. Different weight ratios between FA and PCN-777 (FA/PCN-777 weight ratio of 1/10, 1/5, and 2/5) were investigated separately to optimize the loading parameters. Then, the mixture was centrifuged (11,000 rpm, 10 min) and washed three times with DMF to remove excessive free FA ligands. We quantified the amount of FA installed on the PCN-777 NPs surface by reading the characteristic absorption band of FA at 280 nm using UV-vis. Subsequently, 1 mL INS solution (10 mg/mL, dissolved in dilute HCl, pH 3.0) was added dropwise to 20 mL F-P NPs dispersion (0.5 mg/mL in ddH_2O) and stirred for 12 h at room temperature to obtain I@F-P NPs. Different feeding ratios (INS: PCN-777 NPs = 3:1, 2:1, 1:1, 1:2, 1:3) were also investigated. The resulting mixture was purified by centrifugation three times to remove free INS. The absorbance of FA saturated solution and MOF supernatant was measured by BCA assay. The INS content retained in FA-modified PCN-777 NPs was quantified by BCA protein assay and TGA (TGA 50).

The obtained PCN-777 NPs, F-P NPs, I@P NPs, and I@F-P NPs were characterized by the Malvern Zetasizer Nano series ZS-90 to measure the hydrodynamic size and zeta potential. The TEM tests were performed using a Hitachi H-7000FA TEM to evaluate the morphology of all samples. The EDS elemental mapping analysis was performed using the FEI Talos F200X. PXRD was carried out with a Rigaku MiniFlex 600 X-ray diffractometer under Cu Kα radiation (parameters: 600 W). UV-vis spectroscopy was measured by a UV-vis spectrophotometer (UV-2600, Shimadzu). The fluorescence signal of the PCN-777-based nanosystems was detected by a fluorescence spectrophotometer (RF-6000, Shimadzu). CLSM images were collected by the Carl Zeiss NOL-LSM 710.

FA LC was calculated by Equation 1:

$$\text{LC} = (\text{total weight of FA} - \text{weight of supernatant FA}) / \times \text{weight of PCN-777} \times 100\% \quad \text{(Equation 1)}$$

INS LC was calculated by Equation 2:

$$\text{LC} = (\text{total weight of INS} - \text{weight of supernatant INS}) / \times \text{weight of PCN-777} \times 100\% \quad \text{(Equation 2)}$$

INS loading content was calculated by Equation 3:

$$\begin{aligned}\text{Loading content} = {} & (\text{total weight of INS} \\ & - \text{weight of supernatant INS}) / \\ & \times (\text{weight of PCN-777} + \text{total weight of INS} \\ & - \text{weight of supernatant INS} + \text{total weight of FA} \\ & - \text{weight of supernatant FA}) \times 100\%\end{aligned} \quad \text{(Equation 3)}$$

In vitro stability

The procedures to quantify the PCN-777-based nanosystem stability and INS degradation by the enzyme were conducted as described previously.[37] Briefly, the different formulations were respectively dispersed in ddH_2O, DMEM cell medium containing 10% fetal bovine serum (FBS), and the size at various time points was measured by DLS. As for the protective performance determination of the PCN-777-based nanosystem on INS in enzyme, the NPs were incubated in simulated intestinal fluid containing trypsin (1 mg/mL) at 37°C for 3 h. At different time intervals, aliquots of 100 μL were taken out and 200 μL DMSO containing 0.1% trifluoroacetic acid was added to quench the enzymatic reaction. The NPs were then completely disrupted using PBS, and the concentration of INS was determined via a bovine INS ELISA kit.

To investigate whether the bioactivity of INS was maintained after preparation, long-term storage, and drug release, I@P NPs and I@F-P NPs after 2 months of synthesis were immersed in PBS at 37°C for 48 h and then separated by ultracentrifugation. The amount of INS released in the supernatant was determined using a BCA protein assay kit. Subsequently, the quantified amount of released INS (5 IU/kg) or free INS (5 IU/kg) was administered to Sprague-Dawley rats fasted overnight by subcutaneous injection, and blood glucose changes were detected using a glucometer. In addition, the released INS and free INS were taken for CD determination to evaluate the changes in the secondary structure of INS.

Release kinetics

To test the release profiles of INS from I@P NPs and I@F-P NPs, different INS-loaded formulations were placed in dialysis bags

(molecular weight cutoff 10 kDa) and dispersed in FaSSGF, FaSSIF (without phosphate), and PBS at 37°C for 48 h. At different time points, 100 μL buffer solution was taken for testing, and an equal volume of fresh buffer solution was added to keep the volume constant. The quantity of INS was determined using the BCA protein assay kit. Furthermore, we simulated the physiological environment of I@P NPs and I@F-P NPs after oral administration by dialyzing the NPs in FaSSGF for 2 h and then in FaSSIF for another 2 h and PBS (pH 7.4) for an additional 44 h. Sampling and INS concentration detection were carried out as described in the above methods. Additionally, we acquired TEM and SEM images of I@P NPs and I@F-P NPs incubated in PBS for various time intervals. We also determined the PXRD patterns of the nanosystems following incubation to assess the disintegration of the I@F-P NPs.

Hemolysis test

Rat blood samples were incubated with different concentrations of I@F-P NPs in saline solution (0.05, 0.1, 0.2, 0.3, and 0.5 mg/mL) at 37°C for 4 h. The groups in which erythrocytes were incubated with H_2O and saline were set as the positive control and the negative control. After 4 h of incubation, the samples were centrifuged, the supernatant was measured at 540 nm using UV-vis, and the hemolysis rate of the samples was calculated using Equation 4:

$$\text{Hemolysis} = (\text{A samples} - \text{A negative})/(\text{A positive} - \text{A negative}) \times 100\%. \quad \text{(Equation 4)}$$

Cell culture

The human colon adenocarcinoma cell line (Caco-2), the murine colorectal carcinoma cell line (CT-26), and the human normal liver cell line (L02) were purchased from the China Type Culture Collection. CT-26 cells and L02 cells were cultured in DMEM supplemented with 10% FBS (20% required for Caco-2) and 1% penicillin/streptomycin in an atmosphere of 5% CO_2 at 37°C.

In vitro cytotoxicity and live/dead assay

In vitro cytotoxicity was assessed using an MTT assay in Caco-2 cells, CT-26 cells, and L02 cells, and a live/dead cell assay. Different cell lines were separately cultured in 96-well plates at a density of 1×10^4 cells/well. The cells were then incubated with 100 μL PCN-777 NPs, I@P NPs, and I@F-P NPs at concentrations of 0, 31.25, 62.5, 125, 250, and 500 μg/mL in DMEM, respectively, and 5 samples were taken in parallel. After 24 h of incubation, the cells were exposed to 100 μL freshly prepared MTT solution (5 mg/mL) for another 4 h. Afterward, the supernatant was carefully removed, and DMSO (100 μL) was added to each well. The optical density was measured at 490 nm using Microplate Reader. The live/dead assay was performed by staining Caco-2 cells following PCN-777-based nanosystems (500 μg/mL) administration with 100 μL PBS buffer containing calcein acetoxymethyl ester (Calcein AM) and propidium iodide (PI). Finally, the cells were observed by an inverted fluorescence microscope.

Cell western blot analysis

Caco-2 cells were seeded in 12-well plates with slides at a density of 1×10^5 cells per well overnight and subsequently treated with or without myricetin solution (150 mmol/L) in a similar way to the PCFT low-expression group or high-expression group in the earlier-reported procedure. Protein extraction was performed after treating the cells with radioimmunoprecipitation assay (RIPA) lysis buffer, and the protein concentration was determined using the BCA assay. The extracted proteins were then separated by electrophoresis on 12% sodium dodecyl sulfate-polyacrylamide gel electrophoresis (SDS-PAGE). After protein transfer and blocking, incubation with rabbit anti-PCFT (HCP1) antibodies was carried out overnight at 4°C, followed by a 30-min incubation with goat anti-rabbit IgG-HRP at room temperature. After washing the membranes with Tris-buffered saline four times, the protein bands were detected using an enhanced chemiluminescence reagent.

Cellular internalization studies *in vitro*

To estimate the internalization of NPs in the PCFT high- and low-expression groups, Caco-2 cells or myricetin pre-treated Caco-2 cells were incubated with free R-I, R-I@P NPs, and R-I@F-P NPs with different modification densities of FA (hereafter referred to as I@F-P NPs [1:10, 1:5, 2:5]) at 37°C for different time intervals. The cells were further fixed with 4% paraformaldehyde and stained with DAPI for 20 min. The cell internalization of PCN-777-based nanosystems was visualized by CLSM (LSM 800, Carl Zeiss) and was also quantitively measured using flow cytometry. The three-dimensional visualization was conducted by the z stack method.

To further identify the uptake mechanisms of I@F-P NPs in the PCFT high- and low-expression groups, Caco-2 cells were treated with R-I@F-P NPs under hypothermia or co-incubated with various inhibitors (lovastatin [1 mg/mL], methyl-β-cyclodextrin [10 mmol/L], filipin [1 mg/mL], chlorpromazine [10 mg/mL], and cytochalasin D [1 mg/mL]) at 37°C. After incubation for 4 h, the internalized amounts of I@F-P were visualized by CLSM and quantified using flow cytometry.

To elucidate the intracellular trafficking of NPs, Caco-2 cells were incubated with I@P NPs and I@F-P NPs (1:10, 1:5, 2:5) for 4 h at 37°C. Subsequently, Caco-2 cells were stained with Lyso-Tracker Green or Golgi-Tracker Green for 30 min. Co-localization of samples and lysosomes/Golgi was detected using CLSM.

Transepithelial transport studies

The transepithelial transport studies were conducted following previously reported procedures.[37] In short, the Caco-2 cells were cultured in transwell inserts for 21 days until the transepithelial electrical resistance (TEER) values exceeded 500 $\Omega \times cm^2$. Caco-2 cell monolayers with high or low expression of PCFT were co-incubated with free INS and I@P NPs and I@F-P NPs on the apical side for 48 h. A total of 100 μL of the sample was taken out from the basolateral side at different time intervals, and 100 μL of DMEM was always supplemented to maintain a consistent volume. TEER values were measured at various time points to determine tight junction integrity during the drug administration process. After 48 h of incubation,

samples of the apical and basolateral layers were collected, respectively, and the cell monolayer was lysed with RIPA lysate and collected. The INS contents in each sample were then tested utilizing the bovine INS ELISA kit. The following equation was utilized to calculate the Papp from the different treatments:

$$P_{app} = \frac{dQ}{dt} \times \frac{1}{A \times C_0}, \quad \text{(Equation 5)}$$

where dQ/dt is the flux of INS from the apical side to the basolateral side, A is the membrane area (cm^2), and C_0 is the initial concentration of INS on the apical side.

In addition, the degradation rates of INS in different preparations were calculated according to Equation 6:

$$\text{Degradation\%} = \frac{m(\text{total}) - m(\text{apical}) - m(\text{basolateral}) - m(\text{inside})}{m(\text{total}) - m(\text{basolateral})} \times 100\% \quad \text{(Equation 6)}$$

where m(total) is the total mass of INS added, m(apical) is the mass of INS in the apical layer, m(basolateral) is the mass of INS in the basolateral layer, and m(inside) is the mass of INS in the cell monolayer.

To intuitively illustrate the efficiency of transcellular transport of PCN-777-based nanosystems, we seeded Caco-2 cells on the basolateral side and used RITC-labeled INS preparations to co-incubate cell monolayers on the apical side. After 48 h, the fluorescence distributions on the apical and basolateral sides were observed using the SI Imaging Amix imaging system. Next, to verify that the NPs maintained its intact morphology after penetrating the cell monolayer via a Golgi-mediated pathway, we collected samples of I@P NPs and I@F-P NPs from the basolateral side at 24 h and obtained TEM images after centrifugation.

In addition, the deep penetration of I@F-P NPs between different cell batches was studied as reported in the literature.[60] Caco-2 cells in batch 1 were cultured in a medium that contained different INS formulations for 12 h. Then, batch 1 was put into fresh culture medium containing cells from batch 2 for 12 h. The above step was repeated to obtain batch 3. The above three different cell batches were observed by CLSM.

Animal models and diabetes induction

Male Sprague-Dawley rats (180–200 g) and BALB/c mice (18–20 g) were provided by Beijing Vital River Laboratory Animal Technology. New Zealand rabbits (2–2.5 kg) were provided by Hubei Yizhicheng Biological Technology. All the animal studies were conducted following the Chinese Regulations for the Administration of Affairs Concerning Experimental Animals and performed in compliance with the guidelines of the Institutional Animal Care and Use Committee of Wuhan University. To establish an alloxan-induced diabetic rat model, healthy rats were intravenously injected with alloxan 50 mg/kg once and the blood glucose changes were monitored daily to confirm the rats' diabetic status. After 7 days, the blood glucose was stable at 20 mmol/L, proving the diabetes model was successfully established. The difference between the establishment of diabetes models of mice and rabbits was that the dosage of alloxan in mice and rabbits is 100 mg/kg. If the BGL of rabbits did not rise after the first injection, 100 mg/kg alloxan would be injected again through the ear vein 48 h later.

Western blot analysis

Tissue samples from various segments of the intestines were collected from both euthanized diabetic and normal mice. Intestinal cells were isolated following established protocols.[44] Subsequently, protein extraction was performed, and protein concentrations were determined using the BCA assay. The extracted proteins were then separated by electrophoresis on 12% SDS-PAGE. After protein transfer and blocking, the incubation of proteins and antibodies and the detection of protein bands were performed according to the above steps.

Immunofluorescence staining

Immunofluorescence staining was used to analyze the expression of PCFT in the intestinal villi of diabetic and normal mice. Frozen sections of duodenum tissue were prepared using a cryostat (RM2016). These sections were blocked with PBS containing 1% bovine serum albumin. Immunofluorescence staining was performed using rabbit PCFT (HCP1) antibody and secondary antibody, which was fluorescently labeled goat anti-rabbit IgG. Subsequently, DAPI staining was applied, and the expression of PCFT was visualized using the scanner (Pannoramic SCAN).

In vivo fluorescence imaging

R-I, R-I@P NPs, and R-I@F-P NPs were orally administered to the overnight fasted diabetic mice or normal mice. The SI Imaging Amix imaging system was used to assess the distribution and metabolism of INS preparations in mice with different PCFT intestinal expressions at different time points. Another group of diabetic mice or normal mice was sacrificed 12 h after R-I, R-I@P NP, and R-I@F-P NP treatment, and the organs and intestines were collected and observed. The same procedure was done with diabetic rats. The intestine loops of the R-I, R-I@P NPs, and R-I@F-P NPs medicated rats were collected by the same procedure and frozen in Tissue-Tek OCT with liquid nitrogen. Intestinal sections were obtained using a cryostat and visualized by CLSM after staining with DAPI for 10 min.

Tracking nanoparticle diffusion in the small intestine

The rats were sacrificed 4 h after oral administration of different preparations, and the small intestines were collected and

washed with PBS. Samples were serially fixed in 0.1 M phosphate buffer containing 2.5% glutaraldehyde and 4% osmium tetroxide solution and then were transferred to a Beem embedding capsule. Micro-embedding resin was added to the embedded samples to obtain blocks, which were further sectioned with ultramicrotomy, and these sections were retrieved through a copper grid and then visualized under TEM.

INS bioactivity *in vivo*

In vivo studies were performed in alloxan-induced diabetic rats (n = 5 per group) and rabbits (n = 3 per group). The rats were fasted overnight before experiments and then administered different preparations (free INS, I@P NPs, I@F-P NPs, 50 IU/kg) by gavage and free INS (5 IU/kg) by subcutaneous injection. The rabbits were administrated by gavage with free INS or I@F-P NPs at a dosage of 30 IU/kg. At predetermined time intervals, blood samples were collected for glucose testing using a blood glucose meter. The serum INS level was determined using a bovine INS ELISA kit. During the experiment, the rats drank water arbitrarily and were fed at 12 and 36 h, and the rabbits were fed at 5, 10, 12, 28, and 36 h, respectively.

Long-term safety of consecutive dosing

Mice received oral gavage with free-INS, I@P NPs, and I@F-P NPs (INS at a concentration of 50 IU/kg) once every 2 days for 14 and 30 consecutive days. Mice were then sacrificed after blood collection (for blood routine analysis and blood biochemical indicators measurement), and organs and intestines were soaked in 4% (w/v) formalin and then embedded in paraffin. The tissue was sectioned and stained with H&E for microscopic examination. We conducted an acute toxicity experiment on I@F-P NPs in mice. After an overnight fasting period, the mice were administered orally F-P NPs (quantitated as PCN-777) at doses of 100, 500, 1,000, and 2,000 mg/kg. The body weight and survival status of the mice were continuously monitored over a 14-day period. Following the observation period, the mice were euthanized, and major organs were subjected to H&E staining experiments. Furthermore, the distribution, metabolic pathways, and residual presence of Zr elements in mice were investigated. Both diabetic and non-diabetic mice received I@F-P NPs (INS at a concentration of 50 IU/kg) every 2 days over a 14-day period. After 1 week, the major organs of the mice were collected and subjected to digestion, and the Zr element content was quantitatively determined using inductively coupled plasma-mass spectrometry. In addition, mice were administered orally PBS and I@F-P NPs (INS at a concentration of 50 IU/kg) once every 2 days for a consecutive duration of 30 days. Subsequently, serum samples were collected, and pro-inflammatory cytokines (interferon-γ, IL-1β, TNF-α) were assessed using an ELISA kit.

Statistical analysis

Statistical analysis was determined by a two-tailed Student's t test using the software Prism. $^{*}p < 0.05$, $^{**}p < 0.01$, $^{***}p < 0.001$, and $^{****}p < 0.0001$ were considered statistically significant. All of the results presented were means ± SDs.

RESOURCE AVAILABILITY

Lead contact

Requests for further information, resources, and reagents should be directed to and will be fulfilled by the lead contact, Jian Tian (jian.tian@whu.edu.cn).

Materials availability

This study did not generate new unique reagents.

Data and code availability

All relevant data are included in the paper and the supplemental information. All data reported in this paper will be shared by the lead contact upon request.

ACKNOWLEDGMENTS

This work was financially supported by the following funding agencies: National Natural Science Foundation of China (no. NSFC 22271222, to J.T.), National Natural Science Foundation of China (no. NSFC 21871214, to J.T.), and the Robert A. Welch Foundation (no. B-0027, to S.M.).

AUTHOR CONTRIBUTIONS

J.T. and S.M. designed the research and supervised the study; J.-J.Z., Q.C., and Y.Z. performed the research; J.-J.Z., J.P., and X.Q. analyzed the data; W.T. provided valuable suggestions; and J.-J.Z., J.P., S.M., and J.T. wrote the paper.

DECLARATION OF INTERESTS

The authors have filed a provisional patent related to the sustained-release MOF nanoparticles in this work.

SUPPLEMENTAL INFORMATION

Supplemental information can be found online at https://doi.org/10.1016/j.matt.2024.101948.

Received: August 13, 2024
Revised: November 11, 2024
Accepted: December 17, 2024
Published: January 14, 2025

REFERENCES

1. Cao, Y., Rewatkar, P., Wang, R., Hasnain, S.Z., Popat, A., and Kumeria, T. (2021). Nanocarriers for oral delivery of biologics: small carriers for big payloads. Trends Pharmacol. Sci. *42*, 957–972. https://doi.org/10.1016/j.tips.2021.08.005.
2. Durán-Lobato, M., Niu, Z., and Alonso, M.J. (2020). Oral delivery of biologics for precision medicine. Adv. Mater. *32*, e1901935. https://doi.org/10.1002/adma.201901935.
3. Brown, T.D., Whitehead, K.A., and Mitragotri, S. (2019). Materials for oral delivery of proteins and peptides. Nat. Rev. Mater. *5*, 127–148. https://doi.org/10.1038/s41578-019-0156-6.
4. Hamman, J.H., Enslin, G.M., and Kotzé, A.F. (2005). Oral delivery of peptide drugs - Barriers and developments. BioDrugs *19*, 165–177. https://doi.org/10.2165/00063030-200519030-00003.
5. Hirsch, I.B. (1999). Type 1 diabetes mellitus and the use of flexible insulin regimens. Am. Fam. Physician *60*, 2343–2356.
6. Aronson, R. (2012). The role of comfort and discomfort in insulin therapy. Diabetes Technol. Therapeut. *14*, 741–747. https://doi.org/10.1089/dia.2012.0038.
7. Berlin, I., Bisserbe, J.C., Eiber, R., Balssa, N., Sachon, C., Bosquet, F., and Grimaldi, A. (1997). Phobic symptoms, particularly the fear of blood and

injury, are associated with poor glycemic control in type I diabetic adults. Diabetes Care *20*, 176–178. https://doi.org/10.2337/diacare.20.2.176.

8. Zambanini, A., Newson, R.B., Maisey, M., and Feher, M.D. (1999). Injection related anxiety in insulin-treated diabetes. Diabetes Res. Clin. Pract. *46*, 239–246. https://doi.org/10.1016/s0168-8227(99)00099-6.
9. Lamson, N.G., Berger, A., Fein, K.C., and Whitehead, K.A. (2020). Anionic nanoparticles enable the oral delivery of proteins by enhancing intestinal permeability. Nat. Biomed. Eng. *4*, 84–96. https://doi.org/10.1038/s41551-019-0465-5.
10. Bienvenu, O.J., and Eaton, W.W. (1998). The epidemiology of blood-injection-injury phobia. Psychol. Med. *28*, 1129–1136. https://doi.org/10.1017/s0033291798007144.
11. Yu, J., Wang, J., Zhang, Y., Chen, G., Mao, W., Ye, Y., Kahkoska, A.R., Buse, J.B., Langer, R., and Gu, Z. (2020). Glucose-responsive insulin patch for the regulation of blood glucose in mice and minipigs. Nat. Biomed. Eng. *4*, 499–506. https://doi.org/10.1038/s41551-019-0508-y.
12. Banerjee, A., Ibsen, K., Brown, T., Chen, R., Agatemor, C., and Mitragotri, S. (2018). Ionic liquids for oral insulin delivery. Proc. Natl. Acad. Sci. USA *115*, 7296–7301. https://doi.org/10.1073/pnas.1722338115.
13. Yun, Y., Cho, Y.W., and Park, K. (2013). Nanoparticles for oral delivery: targeted nanoparticles with peptidic ligands for oral protein delivery. Adv. Drug Deliv. Rev. *65*, 822–832. https://doi.org/10.1016/j.addr.2012.10.007.
14. Brayden, D.J., Hill, T.A., Fairlie, D.P., Maher, S., and Mrsny, R.J. (2020). Systemic delivery of peptides by the oral route: Formulation and medicinal chemistry approaches. Adv. Drug Deliv. Rev. *157*, 2–36. https://doi.org/10.1016/j.addr.2020.05.007.
15. Anderson, S.L., Beutel, T.R., and Trujillo, J.M. (2020). Oral semaglutide in type 2 diabetes. J. Diabet. Complicat. *34*, 107520. https://doi.org/10.1016/j.jdiacomp.2019.107520.
16. Overgaard, R.V., Navarria, A., Ingwersen, S.H., Bækdal, T.A., and Kildemoes, R.J. (2021). Clinical Pharmacokinetics of Oral Semaglutide: Analyses of Data from Clinical Pharmacology Trials. Clin. Pharmacokinet. *60*, 1335–1348. https://doi.org/10.1007/s40262-021-01025-x.
17. Xiao, Y., Tang, Z., Wang, J., Liu, C., Kong, N., Farokhzad, O.C., and Tao, W. (2020). Oral insulin delivery platforms: Strategies to address the biological barriers. Angew. Chem., Int. Ed. Engl. *59*, 19787–19795. https://doi.org/10.1002/anie.202008879.
18. Haddadzadegan, S., Dorkoosh, F., and Bernkop-Schnürch, A. (2022). Oral delivery of therapeutic peptides and proteins: Technology landscape of lipid-based nanocarriers. Adv. Drug Deliv. Rev. *182*, 114097. https://doi.org/10.1016/j.addr.2021.114097.
19. Torres-Lugo, M., García, M., Record, R., and Peppas, N.A. (2002). Physicochemical behavior and cytotoxic effects of p(methacrylic acid-g-ethylene glycol) nanospheres for oral delivery of proteins. J. Contr. Release *80*, 197–205. https://doi.org/10.1016/s0168-3659(02)00027-5.
20. Wu, J., Zheng, Y., Liu, M., Shan, W., Zhang, Z., and Huang, Y. (2018). Biomimetic viruslike and charge reversible nanoparticles to sequentially overcome mucus and epithelial barriers for oral insulin delivery. ACS Appl. Mater. Interfaces *10*, 9916–9928. https://doi.org/10.1021/acsami.7b16524.
21. Wang, A., Yang, T., Fan, W., Yang, Y., Zhu, Q., Guo, S., Zhu, C., Yuan, Y., Zhang, T., and Gan, Y. (2019). Protein corona liposomes achieve efficient oral insulin delivery by overcoming mucus and epithelial barriers. Adv. Healthcare Mater. *8*, e1801123. https://doi.org/10.1002/adhm.201801123.
22. Zhu, X., Wu, J., Shan, W., Tao, W., Zhao, L., Lim, J.-M., D'Ortenzio, M., Karnik, R., Huang, Y., Shi, J., and Farokhzad, O.C. (2016). Polymeric nanoparticles amenable to simultaneous installation of exterior targeting and interior therapeutic proteins. Angew. Chem., Int. Ed. Engl. *55*, 3309–3312. https://doi.org/10.1002/anie.201509183.
23. Fang, H., Chen, L., Deng, Z., Gao, Y., Yang, Y., Chen, Q., and Liu, Z. (2023). In situ polymerization of zwitterions on therapeutic proteins to enable their effective oral delivery. ACS Nano *17*, 1128–1143. https://doi.org/10.1021/acsnano.2c08434.
24. Xiao, Y., Tang, Z., Huang, X., Joseph, J., Chen, W., Liu, C., Zhou, J., Kong, N., Joshi, N., Du, J., and Tao, W. (2021). Glucose-responsive oral insulin delivery platform for one treatment a day in diabetes. Matter *4*, 3269–3285. https://doi.org/10.1016/j.matt.2021.08.011.
25. Li, S., Liang, N., Yan, P., Kawashima, Y., and Sun, S. (2021). Inclusion complex based on N-acetyl-L-cysteine and arginine modified hydroxypropyl-beta-cyclodextrin for oral insulin delivery. Carbohydr. Polym. *252*, 117202. https://doi.org/10.1016/j.carbpol.2020.117202.
26. Verma, A., Sharma, S., Gupta, P.K., Singh, A., Teja, B.V., Dwivedi, P., Gupta, G.K., Trivedi, R., and Mishra, P.R. (2016). Vitamin B12 functionalized layer by layer calcium phosphate nanoparticles: A mucoadhesive and pH responsive carrier for improved oral delivery of insulin. Acta Biomater. *31*, 288–300. https://doi.org/10.1016/j.actbio.2015.12.017.
27. Sarmento, B., Martins, S., Ferreira, D., and Souto, E.B. (2007). Oral insulin delivery by means of solid lipid nanoparticles. Int. J. Nanomed. *2*, 743–749. https://doi.org/10.2147/IJN.S2.4.743.
28. He, H., Wang, P., Cai, C., Yang, R., and Tang, X. (2015). VB12-coated Gel-Core-SLN containing insulin: Another way to improve oral absorption. Int. J. Pharm. *493*, 451–459. https://doi.org/10.1016/j.ijpharm.2015.08.004.
29. Ji, K., Wei, X., Kahkoska, A.R., Zhang, J., Zhang, Y., Xu, J., Wei, X., Liu, W., Wang, Y., Yao, Y., et al. (2024). An Orally Administered Glucose-Responsive Polymeric Complex for High-Efficiency and Safe Delivery of Insulin in Mice and Pigs. Nat. Nanotechnol. *19*, 1880–1891. https://doi.org/10.1038/s41565-024-01764-5.
30. Dai, L., Yao, M., Fu, Z., Li, X., Zheng, X., Meng, S., Yuan, Z., Cai, K., Yang, H., and Zhao, Y. (2022). Multifunctional metal-organic framework-based nanoreactor for starvation/oxidation improved indoleamine 2,3-dioxygenase-blockade tumor immunotherapy. Nat. Commun. *13*, 2688. https://doi.org/10.1038/s41467-022-30436-y.
31. Sun, Y., Zheng, L., Yang, Y., Qian, X., Fu, T., Li, X., Yang, Z., Yan, H., Cui, C., and Tan, W. (2020). Metal–organic framework nanocarriers for drug delivery in biomedical applications. Nano-Micro Lett. *12*, 103. https://doi.org/10.1007/s40820-020-00423-3.
32. Chen, T.-T., Yi, J.-T., Zhao, Y.-Y., and Chu, X. (2018). Biomineralized metal-organic framework nanoparticles enable intracellular delivery and endo-lysosomal release of native active proteins. J. Am. Chem. Soc. *140*, 9912–9920. https://doi.org/10.1021/jacs.8b04457.
33. Wang, Y., Yan, J., Wen, N., Xiong, H., Cai, S., He, Q., Hu, Y., Peng, D., Liu, Z., and Liu, Y. (2020). Metal-organic frameworks for stimuli-responsive drug delivery. Biomaterials *230*, 119619. https://doi.org/10.1016/j.biomaterials.2019.119619.
34. Shao, L., Gao, X., Liu, J., Zheng, Q., Li, Y., Yu, P., Wang, M., and Mao, L. (2022). Biodegradable Metal–Organic-Frameworks-Mediated Protein Delivery Enables Intracellular Cascade Biocatalysis and Pyroptosis In Vivo. ACS Appl. Mater. Interfaces *14*, 47472–47481. https://doi.org/10.1021/acsami.2c14957.
35. Linnane, E., Haddad, S., Melle, F., Mei, Z., and Fairen-Jimenez, D. (2022). The uptake of metal-organic frameworks: a journey into the cell. Chem. Soc. Rev. *51*, 6065–6086. https://doi.org/10.1039/d0cs01414a.
36. Zhou, Y., Chen, Z., Zhao, D., Li, D., He, C., and Chen, X. (2021). A pH-triggered self-unpacking capsule containing zwitterionic hydrogel-coated MOF nanoparticles for efficient oral exendin-4 delivery. Adv. Mater. *33*, e2102044. https://doi.org/10.1002/adma.202102044.
37. Zou, J.-J., Wei, G., Xiong, C., Yu, Y., Li, S., Hu, L., Ma, S., and Tian, J. (2022). Efficient oral insulin delivery enabled by transferrin-coated acid-resistant metal-organic framework nanoparticles. Sci. Adv. *8*, eabm4677. https://doi.org/10.1126/sciadv.abm4677.
38. Chen, Y., Li, P., Modica, J.A., Drout, R.J., and Farha, O.K. (2018). Acid-resistant mesoporous metal-organic framework toward oral insulin delivery: Protein encapsulation, protection, and release. J. Am. Chem. Soc. *140*, 5678–5681. https://doi.org/10.1021/jacs.8b02089.

39. Zhou, Y., Liu, L., Cao, Y., Yu, S., He, C., and Chen, X. (2020). A nanocomposite vehicle based on metal-organic framework nanoparticle incorporated biodegradable microspheres for enhanced oral insulin delivery. ACS Appl. Mater. Interfaces *12*, 22581–22592. https://doi.org/10.1021/acsami.0c04303.

40. Feng, L., Wang, K.-Y., Day, G.S., Ryder, M.R., and Zhou, H.-C. (2020). Destruction of metal–organic frameworks: Positive and negative aspects of stability and lability. Chem. Rev. *120*, 13087–13133. https://doi.org/10.1021/acs.chemrev.0c00722.

41. Wang, C., Xiong, C., Li, Z., Hu, L., Wei, J., and Tian, J. (2021). Defect-engineered porphyrinic metal-organic framework nanoparticles for targeted multimodal cancer phototheranostics. Chem. Commun. *57*, 4035–4038. https://doi.org/10.1039/d0cc07903k.

42. Xiao, J., Zhu, Y., Huddleston, S., Li, P., Xiao, B., Farha, O.K., and Ameer, G.A. (2018). Copper metal-organic framework nanoparticles stabilized with folic acid improve wound healing in diabetes. ACS Nano *12*, 1023–1032. https://doi.org/10.1021/acsnano.7b01850.

43. Park, J., Jiang, Q., Feng, D., Mao, L., and Zhou, H.-C. (2016). Size-controlled synthesis of porphyrinic metal-organic framework and functionalization fortargeted photodynamic therapy. J. Am. Chem. Soc. *138*, 3518–3525. https://doi.org/10.1021/jacs.6b00007.

44. Li, J., Zhang, Y., Yu, M., Wang, A., Qiu, Y., Fan, W., Hovgaard, L., Yang, M., Li, Y., Wang, R., et al. (2022). The upregulated intestinal folate transporters direct the uptake of ligand-modified nanoparticles for enhanced oral insulin delivery. Acta Pharm. Sin. B *12*, 1460–1472. https://doi.org/10.1016/j.apsb.2021.07.024.

45. Feng, D., Wang, K., Su, J., Liu, T.-F., Park, J., Wei, Z., Bosch, M., Yakovenko, A., Zou, X., and Zhou, H.-C. (2015). A highly stable zeotype mesoporous zirconium metal-organic framework with ultralarge pores. Angew. Chem., Int. Ed. Engl. *54*, 149–154. https://doi.org/10.1002/anie.201409334.

46. Leal, J., Smyth, H.D.C., and Ghosh, D. (2017). Physicochemical Properties of Mucus and Their Impact on Transmucosal Drug Delivery. Int. J. Pharm. *532*, 555–572. https://doi.org/10.1016/j.ijpharm.2017.09.018.

47. Zhao, Y., Zhao, H., Zhao, X., Qu, Y., and Liu, D. (2020). Synergistic effect of electrostatic and coordination interactions for adsorption removal of cephalexin from water using a zirconium-based metal-organic framework. J. Colloid Interface Sci. *580*, 256–263. https://doi.org/10.1016/j.jcis.2020.07.013.

48. Gao, Y., Suh, M.-J., Kim, J.-H., and Yu, G. (2022). Imparting multifunctionality in Zr-MOFs using the one-pot mixed-linker strategy: The effect of linker environment and enhanced pollutant removal. ACS Appl. Mater. Interfaces *14*, 24351–24362. https://doi.org/10.1021/acsami.2c03607.

49. Hu, G.-B., Xiong, C.-Y., Liang, W.-B., Zeng, X.-S., Xu, H.-L., Yang, Y., Yao, L.-Y., Yuan, R., and Xiao, D.-R. (2018). Highly stable mesoporous luminescence-functionalized MOF with excellent electrochemiluminescence property for ultrasensitive immunosensor construction. ACS Appl. Mater. Interfaces *10*, 15913–15919. https://doi.org/10.1021/acsami.8b05038.

50. Siepmann, J., and Peppas, N.A. (2001). Modeling of drug release from delivery systems based on hydroxypropyl methylcellulose (HPMC). Adv. Drug Deliv. Rev. *48*, 139–157. https://doi.org/10.1016/s0169-409x(01)00112-0.

51. Watanabe, T., Tomioka, N.H., Watanabe, S., Tsuchiya, M., and Hosoyamada, M. (2014). False in Vitro and in Vivo Elevations of Uric Acid Levels in Mouse Blood. Nucleos Nucleot. Nucleic Acids *33*, 192–198. https://doi.org/10.1080/15257770.2013.865742.

52. Lee, D.B.N., Roberts, M., Bluchel, C.G., and Odell, R.A. (2010). Zirconium: biomedical and nephrological applications. Am. Soc. Artif. Intern. Organs J. *56*, 550–556. https://doi.org/10.1097/MAT.0b013e3181e73f20.

53. Zhao, R., Diop-Bove, N., Visentin, M., and Goldman, I.D. (2011). Mechanisms of membrane transport of folates into cells and across epithelia. Annu. Rev. Nutr. *31*, 177–201. https://doi.org/10.1146/annurev-nutr-072610-145133.

54. Furumiya, M., Yamashiro, T., Inoue, K., Nishijima, C., Ohta, K., Hayashi, Y., and Yuasa, H. (2015). Sustained Inhibition of Proton-Coupled Folate Transporter by Myricetin. Drug Metabol. Pharmacokinet. *30*, 154–159. https://doi.org/10.1016/j.dmpk.2014.11.001.

55. Zhang, J., Qin, M., Yang, D., Yuan, L., Zou, X., Dai, W., Zhang, H., Wang, X., He, B., and Zhang, Q. (2021). Nanoprotein interaction atlas reveals the transport pathway of gold nanoparticles across epithelium and its association with Wnt\β-catenin signaling. ACS Nano *15*, 17977–17997. https://doi.org/10.1021/acsnano.1c06452.

56. Kaksonen, M., and Roux, A. (2018). Mechanisms of clathrin-mediated endocytosis. Nat. Rev. Mol. Cell Biol. *19*, 313–326. https://doi.org/10.1038/nrm.2017.132.

57. Peng, S.-F., Tseng, M.T., Ho, Y.-C., Wei, M.-C., Liao, Z.-X., and Sung, H.-W. (2011). Mechanisms of cellular uptake and intracellular trafficking with chitosan/DNA/poly (γ-glutamic acid) complexes as a gene delivery vector. Biomaterials *32*, 239–248. https://doi.org/10.1016/j.biomaterials.2010.08.081.

58. Rennick, J.J., Johnston, A.P.R., and Parton, R.G. (2021). Key principles and methods for studying the endocytosis of biological and nanoparticle therapeutics. Nat. Nanotechnol. *16*, 266–276. https://doi.org/10.1038/s41565-021-00858-8.

59. Fan, W., Xia, D., Zhu, Q., Li, X., He, S., Zhu, C., Guo, S., Hovgaard, L., Yang, M., and Gan, Y. (2018). Functional nanoparticles exploit the bile acid pathway to overcome multiple barriers of the intestinal epithelium for oral insulin delivery. Biomaterials *151*, 13–23. https://doi.org/10.1016/j.biomaterials.2017.10.022.

60. Zhou, Q., Shao, S., Wang, J., Xu, C., Xiang, J., Piao, Y., Zhou, Z., Yu, Q., Tang, J., Liu, X., et al. (2019). Enzyme-activatable polymer–drug conjugate augments tumour penetration and treatment efficacy. Nat. Nanotechnol. *14*, 799–809. https://doi.org/10.1038/s41565-019-0485-z.